A robust method for powder thermal property testing and thermal modeling in additive manufacturing

Chunhui Luo, Peter Andersson, Markus Uhlirsch, Pelle Mellin

Report number: MEF20157

Title	A robust method for powder thermal property testing and thermal modeling in additive manufacturing
Authors	Chunhui Luo, Peter Andersson, Markus Uhlirsch, Pelle Mellin
Publication date	2021-06-14
Report number	MEF20157
Status	Limited distribution
Project number	101506
Business area	Materials Development
Research area	LEGU
Financing	Åforsk
Approved by	2021-06-14

X ⟶

Signerat av: Hans Magnusson

A robust method for powder thermal property testing and thermal modeling in additive manufacturing

Chunhui Luo, Peter Andersson, Markus Uhlirsch, Pelle Mellin

Rapportnummer: MEF20157

Abstract

3D-printing (Additive Manufacturing) of metal materials is growing very fast in various industries such as aircraft, aerospace and biomedical industries. The AM process involves many interacting phenomena including heat transfer, sintering, melting, solidification, fluid flow, phase transformation and microstructure formation. The primary concern is heat and mass transfer mechanisms on both macro and microscopic scales. Conduction in powder is less efficient than in a continuous solid part since conductive transfer can only take place where particles are in physical contact with one another. Accurate information of thermal properties of metal powder in AM is essential for high-fidelity process modeling and simulation. There are little published thermal property data regarding metal powder used for AM. This results in our first objective of developing an experimental method to measure the thermal properties of powder and solid which is tailored to the powder bed condition and an inverse method to obtain the thermal conductivity of powder for the given condition of AM by combining laser flash testing, finite element heat transfer modeling and variables optimization.

On the other hand, computational modeling and simulation methodologies for AM processes have been widely utilized, which is helpful to some extent to the development of AM. The analytic solution of thermal models can offer higher computational performance compared to numerical method like finite element. In this work, the proposed semi-analytic thermal model for powder-bed AM process has been implemented with temperature-dependent material properties. It enables the rapid development, tuning, and evaluation of a control scheme or process parameters without the need for extensive computing time or resources. Furthermore, the developed thermal model has been implemented in the computational tool (MicAM) for AM process. The integrated software facilitates the property calculation, modeling work and the further parameter studies. The results can be visualized in three dimensions, and the size of the molten pool at any scanning time can be measured by using modern 3D graphic technique.

In summary, this project aims at developing a robust method for powder thermal property and thermal modeling enabling fast process parameter development in powder bed additive manufacturing.

Contents

1   Introduction

Additive manufacturing (AM), alternatively named 3D printing, is an advanced and cost-effective manufacturing technology of producing geometrically complex parts [1]. Powder bed fusion (PBF) is a particular type of AM in which the metal powder is melted by a laser or electron beam in a way of layer-by-layer to build new part, generating various technologies (for example, selective laser melting (LB-PBF), electron beam melting (EB-PBF) technology, etc.). To prevent powder oxidation, LB-PBF occurs in inert gas atmosphere (argon or nitrogen), while EB-PBF occurs in vacuum.

The powder bed fusion process involves many interacting phenomena including heat transfer, sintering, melting, solidification, fluid flow, phase transformation and microstructure formation. The primary concern is heat and mass transfer mechanisms on both macro and microscopic scales. The transient nature of heat transfer phenomena and interaction between the layers makes it a complicated multi-physics and multi-scale problem. As a result, the thermal history of a part's manufacturing procedure, which determines its microstructures, mechanical properties and final dimensions, is essential to the whole process. To this end, the thermal modeling of the AM processes can be utilized for optimizing the process parameters without the requirement for time-consuming and costly experiments. These efforts can be classified into three main categories known as experimentation, numerical modeling, and analytical modeling. Thermal modeling requires prior knowledge of the thermal properties of the material.

In this section, first a brief review of the thermal modeling and related thermal properties is given. Then the objective of project is presented.

1.1   Thermal modeling

The thermal modeling can be classified into two main categories known as numerical modeling and analytical modeling. In general, mathematical method is a supplemental route to explore and understand the fundamental behavior in the AM process.

1.1.1   Numerical modeling

Numerical methods (for example, finite element method and finite volume method) are often used for modeling of the thermal history of parts which are manufactured by AM processes. The reviews on numerical simulations for powder bed–based additive manufacturing can be found in [2-9]. The quality of a finite element analysis is strongly affected by the heat transfer mechanism, heat source model, underlying mesh and thermal property data, etc.

Roberts *et al.* [10] predicted the transient temperature field for multiple layers of parts in the LB-PBF process of TiAl6V4 alloy using commercial FE software ANSYS. The model has taken into account the laser energy absorption including the non-linearities produced by temperature-dependent material properties and phase changes.

Li and Gu [11] performed the simulation of temperature fields during LB-PBF of AlSi10Mg powder using the finite element software ANSYS. A planar Gaussian heat source was utilized. The effects of laser power and scan speed on the thermal behavior were investigated. In the simulation, the material was in an initial solid powder state and then fused by the scanned laser beam. The powder thermal properties were then changed as the powder temperature exceeded its melting point during the laser radiation process. The effective thermal conductivity of the powder bed is represented by a simplified generic relationship [12]

$$k_p = k_s(1 - \varphi) \tag{1}$$

where k_p and k_s are the thermal conductivities of powder bed and solid materials, φ the porosity of the powder bed.

Du *et al.* [13] also developed a model to calculate the temperature field of AlSi10Mg molten pool in LB-PBF process using finite element software ANSYS. The thermal properties of the material and the variation of laser power absorptivity with temperature were taken into account; the laser heat source was regarded as a 3D Gaussian body heat source, and successfully implemented that the element properties of the material were transformed from powder state to solid state in real time. A similar way for treating thermal conductivity as in [11] was taken.

Andreotta *et al.* [14] presented a sophisticated multi-physics model of the powder bed laser melting additive manufacturing process using finite element software COMSOL, which allows for the direct simulation of fluid flow in addition to thermal transport. This work includes a numerical model that was validated with in-house experiments, as well as experimental determination of thermal conductivity of gas-atomized Inconel 718 powder particles.

Denlinger *et al.* [15] developed a finite element modeling strategy to allow for thermo-elastoplastic modeling of multi-layer LPBF builds, which takes into account the melting and solidification of each powder layer and assigns the appropriate material properties accordingly. The conductivity k_p of the Inconel 718 powder is expressed as known powder-solid relationship [16]

$$k_p = k_f \left[\left(1 - \sqrt{1-\varphi} \right) \left(1 + \varphi \frac{k_r}{k_f} \right) + \sqrt{1-\varphi} \left(\frac{2}{1-k_f/k_s} \left(\frac{2}{1-k_f/k_s} ln \frac{k_s}{k_f} - 1 \right) + \frac{k_r}{k_f} \right) \right] (2)$$

where k_p and k_s are the thermal conductivities of powder bed and solid materials, φ the porosity of the powder bed, k_f the thermal conductivity of the argon gas surrounding the particles. k_r is heat transfer attributed to the radiation between the individual sphere of the materials and given as

$$k_r = \frac{4}{3}\sigma T^3 D_p \tag{3}$$

where D_p is the average diameter of the powder particles, σ the Stefan–Boltzmann constant, T the temperature.

Promoppatum *et al*. [17] invetsigated the thermal behavior in parts made from Inconel 718 by LB-PBF using both an analytical solution (the Rosenthal equation) and the FE method (COMSOL). It was found that the FE model is more accurate at a high energy input because it incorporates more realistic material properties.

Li *et al*. [18] used finite element software ANSYS to simulate the thermal behaviour and melt pool dimensions of parts in the SLM process of AlSi10Mg alloy point exposure scan and to predict the relationship between processing parameters and microstructure defects. The effective thermal conductivity of powder k_p is calcuated using the the following relation

$$k_p = k_s \frac{\rho_r n}{\pi} x \tag{4}$$

where k_s is the thermal conductivity of the solid materials, ρ_r the relative density of the powder bed assigned as 0.6, n the coordination number equal to 6, and x the contact size ratio.

1.1.2 Analytical modeling

One of the main drawbacks of finite element method is the large computational cost even through some commercial software can speed up the computation using special mesh technique. Compared to finite element method, analytical solutions for thermal modeling in AM have several advantages: capturing more physical phenomena, high computational efficiency and

easy implementation. These are particularly useful for the control and optimization of the AM process.

Recently, more work regarding thermal field predictions by using physics-based analytical model has been published [19-23]. An exact solution for the heat equation in arbitrary-shaped domains is not available when allowing the material properties to vary as a function of temperature. Instead, the most promising approach is to use a "semi-analytic" solution method.

Plotkowski *et al*. [19] presented a method to rapidly calculate the transient heat transfer in powder bed fusion additive manufacturing using a semi-analytical heat conduction model. The model was verified for LB-PBF of AlSi10Mg and electron beam melting of IN718 powder, and the results were compared with the predicted steady-state equation Rosenthal. Stump and Plotkowski [20] further proposed an adaptive integration technique which is designed for predicting heat conduction around a moving heat source for welding and additive manufacturing. The proposed adaptive algorithm was proved to be more robust and computationally efficient than non-adaptive scheme.

Mirkoohi *et al*. [21] proposed an analytical model to predict the distribution of the temperature profile by considering the interaction of the layers during the laser metal AM process. The material properties are assumed to be temperature dependent, and also the melting/solidification phase change is considered. The predicted temperature from the analytical model for Ti-6Al-4V were compared with the experimental values and FEM results.

Ning *et al*. [22] presented analytical models using two types of heat sources, namely point moving heat source and semi-ellipsoidal moving heat source, to predict the three-dimensional temperature distribution in the LB-PBF process of Ti-6Al-4V.

Forslund *et al*. [23] integrated each segment of the beam path separately using Gaussian quadrature. They found that the required quadrature order to achieve accurate results for a specific path segment depended heavily on the heat flux parameters. Their approach was to iteratively test quadrature orders under various conditions and to generate a look-up table for later use. The downside of this approach is the requirement for pre-calculating the look-up table, and the symmetric distribution of quadrature nodes around the middle of a given path segment does not take advantage of the increasing diffusiveness of the thermal field with increasing conduction times.

Steuben *et al*. [24] found that the utility of existing analytical solutions is limited due to their underlying assumptions, some of which are their derivation based on a homogeneous semi-infinite domain and temperature-independent material properties. An enriched analytic solution method (EASM) was introduced to capture the actual thermal physics associated with the relevant AM processes, which includes the handling of strong nonlinear variations in material properties due to their dependence on temperature, finite non-convex solution domains, behavior of heat sources very near domain boundaries, and mass accretion coupled to the thermal problem. The enriched analytic solution method (EASM) was proved to produce results equivalent to those of numerical methods (such as Finite Element Method).

Huang [25] developed an analytical model for fast process optimization and potentially for real-time process of LB-PBF. The critical physics i.e., the randomly packed powder bed, heat source penetration, melting regime, heat accumulation and volume shrinkage were taken into consideration in the model. A 3D heat source model with variant penetration depths, together with the varying melting regimes, was utilized to solve the transient thermal field. The powder bed was treated as a homogeneous medium with effective thermophysical properties derived from the randomly packed rain model. The proposed model can perform a time-efficient prediction of the localized-transient thermal field, melt pool temperature distribution, and multi-

track overlapping dimension. Experiments with metallic SS 17-4PH powder validated the built model.

Liu *et al*. [26]. Proposed an analytical model for LB-PBF process, which is based on the depression shape of the molten pool front formed under recoil pressure and surface tension and thermal-dynamics balance. Dimensions of the molten pool are calculated through solving the energy equilibrium equations.

1.2   Thermal property

Thermal properties of metal powder include mainly density, enthalpy, heat capacity, and thermal conductivity. There are numerous publications related to the thermal properties of common solid materials [27, 28]. However, the thermal conductivity for powder is most concerned in the present project.

For some commonly used alloys in AM, the thermophysical properties are collected from [9, 29] as listed in Table *1* and Table *2*.

Table 1 Thermophysical properties of commonly used alloys in AM [9, 29]

Properties	Liquidus temperature (K)	Solidus temperature (K)	Density (kg/m3)	Viscosity (kg/m s)	Surface tension (N/m)	dγ/dT (N/m K)
SS316	1733	1693	7800	$7 \times 10{-3}$	1.5	$-0.40 \times 10{-3}$
Ti-6Al-4V	1928	1878	4430	$4 \times 10{-3}$	1.52	$-0.26 \times 10{-3}$
IN718	1609	1533	8100	$5 \times 10{-3}$	1.82	$-0.37 \times 10{-3}$
H13	1725	1585	7900	$7 \times 10{-3}$	1.9	$-0.43 \times 10{-3}$
800H	1675	1608	7270	$7.5 \times 10{-3}$	1.82	$-0.40 \times 10{-3}$
AlSi10Mg	867	831	2670	$1.3 \times 10{-3}$	0.82	$-0.35 \times 10{-3}$
AA6061	925	855	2700	-	-	-

Table 2 Thermal conductivities and specific heats of commonly used alloys in AM [9, 29]

Properties	Thermal conductivity (W/m K)	Specific heat (J/kg K)
Ti-6Al-4V	$1.57 + 1.6 \times 10^{-2} T - 1 \times 10^{-6} T^2$	$492.4 + 0.025 T - 4.18 \times 10^{-6} T^2$
IN718	$0.56 + 2.9 \times 10^{-2} T - 7 \times 10^{-6} T^2$	$360.4 + 0.026 T - 4 \times 10^{-6} T^2$
SS316	$11.82 + 0.0106 T$	$330.9 + 0.563 T - 4.015 \times 10^{-4} T^2 + 9.465 \times 10^{-8} T^3$
H13	$18.29 + 7.5 \times 10^{-3} T$	$341.9 + 0.601 T - 4.04 \times 10^{-4} T^2$
800H	$0.51 + 2.0 \times 10^{-2} T - 6 \times 10^{-6} T^2$	$352.3 + 0.028 T - 3.7 \times 10^{-6} T^2$
AlSi10Mg	$113 + 1.06 \times 10^{-5} T$	$536.2 + 0.035 T$
AA6061	$2.52 + 0.4 \times 10^{-2} T - 7.36 \times 10^{-6} T^2$	$929.0 - 0.627 T - 1.48 \times 10^{-3} T^2$

Also, thermophysical properties over a range of temperature for TiAl6V4 and IN 718 in solid state are shown in Figure 1 and Figure 2, respectively. These data come from the book by Mills [28], which could be used for modeling and simulations.

Even through there are plenty of thermal properties data available for the common solid materials, there still are little published thermal property data regarding powder used for AM.

Nolan *et al*. [30] pointed out that the main consideration of thermal conductivity of metal powders for numerical simulation of AM process is the temperature near the melting point and above in liquid state. A constant thermal conductivity is assumed if there is no experimental data available.

The thermal conductivity of a powder bed in AM process is very different from its solid counterpart since there is limited contact between particles in the loosed packing conditions and powder bed is infiltered with inert gases and vacuum in LB-PBF. It requires accurate data for thermal properties of AM powders. Thümmler [31] proposed that thermal conductivity is

influenced by powder porosity and pore geometries and thermal conductivity is controlled by gas content in the voids of the powder and contact areas.
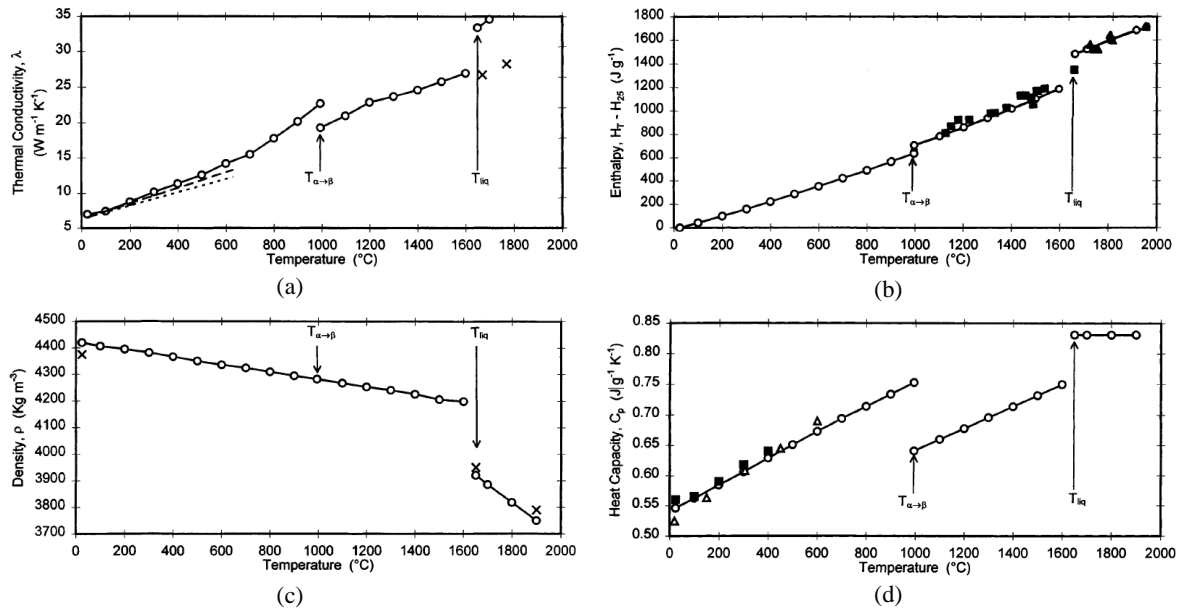

(a)

(b)

(c)

(d)

Figure 1 Thermo physical properties for Ti-alloy (TiAl6V4) as a function of temperature [28]
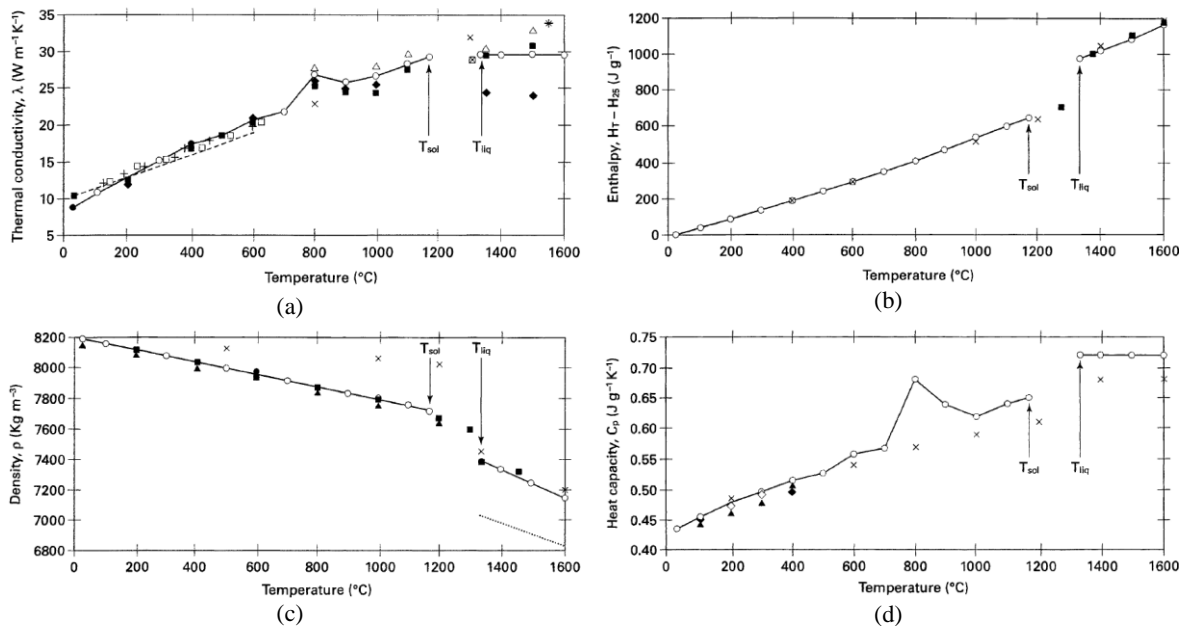

(a)

(b)

(c)

(d)

Figure 2 Thermo physical properties for Nickel-alloy (IN 718) as a function of temperature [29]

1.2.1   Measurement of thermal conductivity

Thermal conductivity methods are broadly classified as either steady-state methods or transient methods. Transient heat transfer methods are capable of directly determining thermal diffusivity, whereas steady-state methods are considered to be more accurate than transient methods for testing dry materials. The transient methods (including laser flash method, transient hot wire method, etc.) are often used for measuring thermal conductivities of AM solids and powders in. Table 3 gives a brief comparison for the methods *c*ommonly used methods and techniques to measure the thermal conductivity [32].

Table 3 Some commonly used methods and techniques to measure the thermal conductivity [32]

Method	Description	Temperature range	Materials	Advantages	Disadvantages
Laser flash	Thermal diffusivity is determined from an analysis of the temperature rise vs. time response induced by absorption of a pulse of laser energy.	−100 - 3000°C	Solids, liquids, and powders	Temperature range, most small specimen, fast, accuracy at high temperature	Expensive
sHot wire	The thermal properties are obtained from the temperature vs. time response due to a heat flux generated by the wire embedded in the specimen.	20 - 2000°C	Plastics, granules, powders	Temperature range, fast, accuracy	Limited to low conductivity materials
Hot disk	The hot disk transient plane source (TPS) method utilizes a plane sensor and a special mathematical model describing the heat conductivity, combined with electronics, enables the method to be used to measure Thermal Transport Properties.	30 - 1200 K	Liquids, pastes, solids and powders	Very short time accuracy, different thermal properties simultaneously	The range of 0.005 and 500 W/(m K)

Wei *et al.* [33] investigated the thermal conductivities of five AM powders (Inconel 718, 17-4 stainless steel, Inconel 625, Ti-6Al-4V, and 316L stainless steel) for the LB-PBF process using the transient hot wire method with different infiltrating gases (argon, nitrogen, and helium) within a temperature range of 295–470 K. Figure 3 shows the temperature dependent thermal conductivities of the powders under argon. It is noted that the maximum temperature of 473 K in these measurements was limited by the melting temperature of the Isonel insulation on the Pt wire.
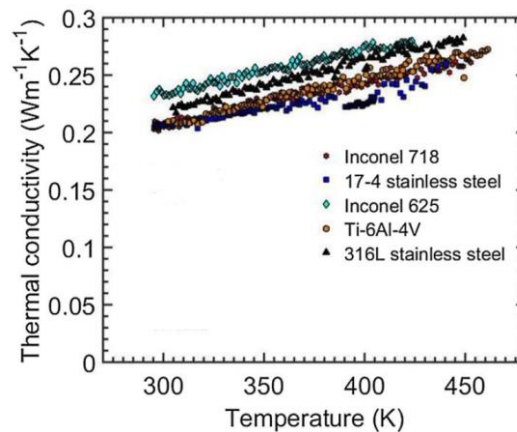

Figure 3 Temperature dependent thermal conductivity of the powders at 101 kPa under argon [32]

National Institute of Standards and Technology (NIST) and the University of Louisville have developed new measurement method for AM solid and powder in order to measure thermal properties of materials using laser flash technique [34-35]. While the additively manufactured powder capsules allow the powder to be captured in a state like its use in the LB-PBF process. The inversely analyzed thermal conductivity values of IN625 and Ti-6Al-4V powders from three different cone samples at various temperatures are shown in Figure 4.
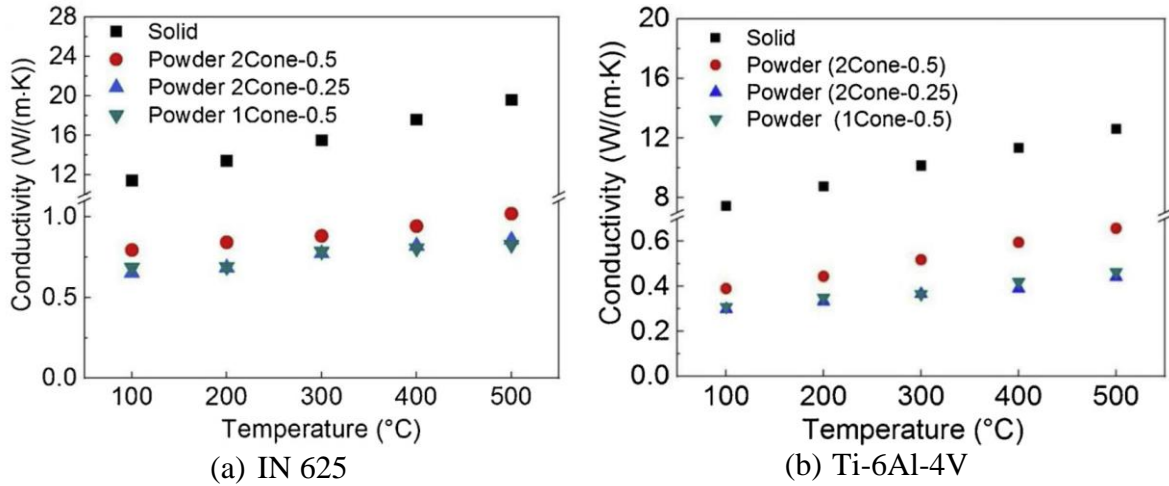
Figure 4 thermal conductivity values of IN625 and Ti-6Al-4V powders at various temperatures

Martínez *et al*. [36] investigated the thermal diffusivity and thermal conductivity of AlSi10Mg obtained by SLM with different relative densities, 99 and 99.5%, in the temperature range from 25 to 400 °C. Laser-flash analysis was used to measure the thermal diffusivity of the specimens using a Netzsch LFA 457 MicroFlash. Figure 5 shows the measured thermal conductivity in the as-built and heat-treated conditions of the XZ specimen (a) and XY specimen (b). The thermal conductivity at room temperature of the as-built LB-PBF samples studied in the work is found to be 115 (99% dense) to 122 (99.5% dense) W/m K, which is similar to the values reported for the die-cast alloys with a similar chemical composition. The anisotropy is attributed to the presence of Si particles along the grain boundaries of columnar grains.
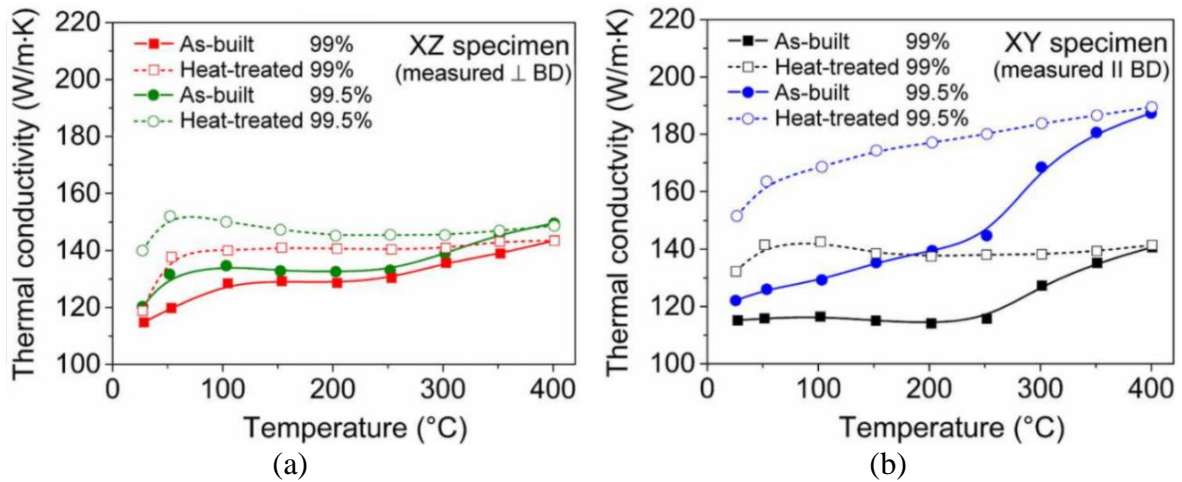

Figure 5 Measured thermal conductivity of AlSi10Mg in the as-built and heat-treated conditions of the XZ specimen (a) and XY specimen (b) after [35]

Andreotta *et al*. [14] measured thermal conductivity of IN 718 using hot disk method with a TPS 2200 scientific instrument. The thermal conductivity vs temperature at various packing density is shown in Figure 6.

Smith *et al*. [37] presented a more comprehensive study of thermal conductivity measurements of Ti-6Al-4V powder (45–106 μm) sintered using a range of electron beam input energies by mean of laser flash analysis. It was intended to investigate to what extent the thermal conductivity of local regions in a titanium Ti-6Al-4V powder bed in EB-PBF could be varied by imparting more energy from the beam. It was found from Figure 7 that the calculated thermal conductivity at two temperatures, 40 and 730 °C, was more than doubled over the range of input

energies explored. The resulting change in thermal conductivity is almost only related to the change in morphology, not the densification of the powder itself.
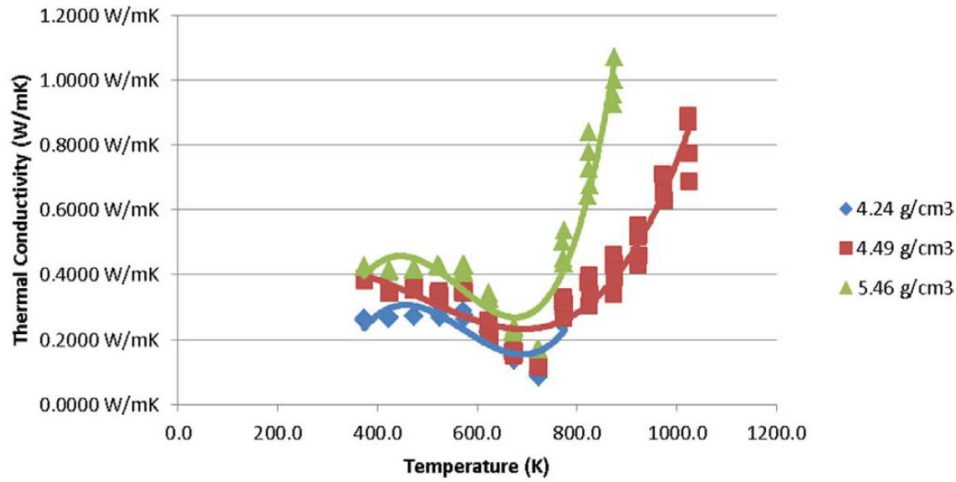

Figure 6 Experimentally determined thermal conductivity of Inconel 718 powder.

1.2.2 Calculation of thermal property

The thermal properties can be obtained from the published papers and books except for direct measurements. An alternative way is to use computational method, for example, CALPHAD method or empirical formula.
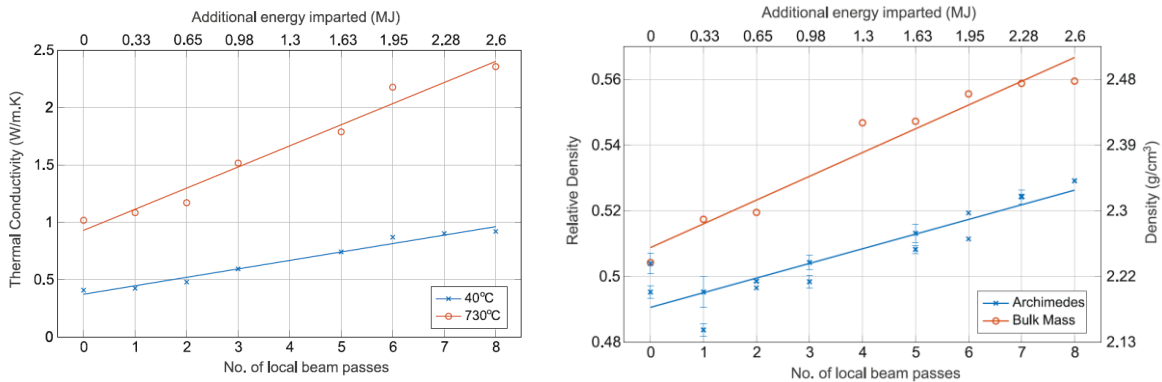

Figure 7 thermal conductivity and density of sintered samples with increasing number of local beam passes: (a) thermal conductivity at 40 and 730 °C; (b) density by direct mass measurement and saturated Archimedes method.

Computational thermodynamics, specifically CALPHAD (CALculation of PHAse Diagrams), can predict thermodynamic properties and phase stability of an alloy under stable and metastable conditions. There are several software based on CALPHAD method (commercial software, e.g. Thermo-Calc®, FactSage®, PANDAT®, MatCalc®, JMatPro®, as well as open-sources codes such as OpenCalphad and PyCalphad).

Hope and Mason [38] presented the application of computational thermodynamics to AM. It was pointed out that the properties such as density, specific heat, and enthalpy can be calculated as a function of composition and temperature using Thermo-Calc® and tailored databases. The thermal conductivity for Al-based and Ni-based alloys can even be calculated using Thermo-Calc with the recent version TCS Al-based or Ni-based Alloy Database [39].

JMatPro® [40] can calculate a wide range of materials properties for alloys and is particularly aimed at multi-component alloys used in industrial practice. For the common-used alloys in

AM, the typical thermal properties (e.g., density, enthalpy, heat capacity, and thermal conductivity) could be calculated using JMatPro® and related database.

1.3   Objective

The objectives of this project are:

1) To develop a method to measure the thermal properties of powder which is tailored to the powder bed condition in LB-PBF or EB-PBF;
2) To develop a method to obtain the thermal conductivity of powder for the given condition of AM by combining laser flash testing, finite element heat transfer modeling and parameter identification;
3) To develop an analytical model to predict temperature with coupling of temperature-dependent thermal properties for a process of LB-PBF or EB-PBF which enables a quick process parameter optimization in powder bed AM.

Based on these objectives, the corresponding tasks and their implementations will be described in Section 2 regarding thermal properties evaluated by combined experimental and numerical method, in Section 3 regarding analytical solution of thermal model, respectively. Additional introduction about the development of robust and fast modeling tool for AM is presented in Section 4. Finally, concluding remarks, future work and knowledge dissemination are given.

2   Thermal properties evaluated by combined experimental and numerical method

2.1   Materials

Two commercial powders INCONEL 718 were selected for testing. The compositions of the powders are listed in Table 4.

Table 4 Compositions of Inconel 718 powders (wt%)

Powder	Ni	Cr	Nb	Fe	Mo	Ti	Mn	Al	Si	C	Co	B
A	54.0	18.5	5.11	Bal	2.91	0.80	0.18	0.51	0.22	0.04	0.01	0.005
B	52.0	18.7	5.08	Bal	3.1	1.05	0.03	0.6	<0.1	0.05	-	-

The particle size distribution PSD was analyzed on carefully split powder samples by laser diffraction ("LD"; Mastersizer 2000, Malvern, UK) and dynamic image analysis ("DIA"; Camsizer XT, Retsch GmbH, Haan, Germany) according to ISO 13322-2:2006. The morphology of the particles was measured by DIA in terms of sphericity SPHT3 (ISO 9276-6) and aspect ratio b/l3, which are calculated according to equations 1 and 2.

$$SPHT_3 = Circularity^2 = \frac{4\pi A}{P^2} \tag{5}$$

where P is the measured perimeter / circumference of a particle projection, A is the measured area covered by a particle projection. For an ideal sphere SPHT is 1, otherwise < 1.

$$b/l_3 = \frac{x_{c\,min}}{x_{Fe\,max}} \tag{6}$$

where $x_{c\,min}$ is the shortest chord of the measured set of maximum chords of a particle projection (for results close to screening/sieving), $x_{Fe\,max}$ the longest Feret diameter out of the measured set of Feret diameters.

Table 5 Rounded results of the particle size and morphology measurements by DIA and LD [41]

Powder	D10 [µm]		D50 [µm]		D90 [µm]		Morphology DIA	
	DIA	LD	DIA	LD	DIA	LD	b/l_3	$SPHT_3$
A	30	32	42	45	56	62	0.86	0.93
B	54	56	70	78	101	110	0.85	0.92

It is found from Table 5 that Powder A is finer (D90DIA = 56 µm) than Powder B (D90DIA = 101 µm). This observation was also reflected in the D10 and D50 values. The aspect ratios and the sphericity of powders show that both Powder A and B are not spherical.

Figure 8 illustrates the particle morphology and surface for the two powders. A decreasing sphericity and surface smoothness from Powder A to Powder B was clearly visible. Particles of Powder A showed a more irregular surface with several sintered/ fused particles, while Powder B consisted of both coarse particles spiked with satellites and big agglomerates formed by smaller particles.

The apparent density, after preparation density, tap density, after vibration density, sintered density and part density of the two powder samples were measured. The results of the performed density evaluations were rounded according to the applicable standards and are listed in Figure 9. The RPA after preparation and vibration density measurement as well as the apparent and tap density measurements showed the same trends: Powder A had larger densities than Powder B. The RPA densities were higher than the corresponding densities measured with conventional methods and the RPA min and max values scattered more.
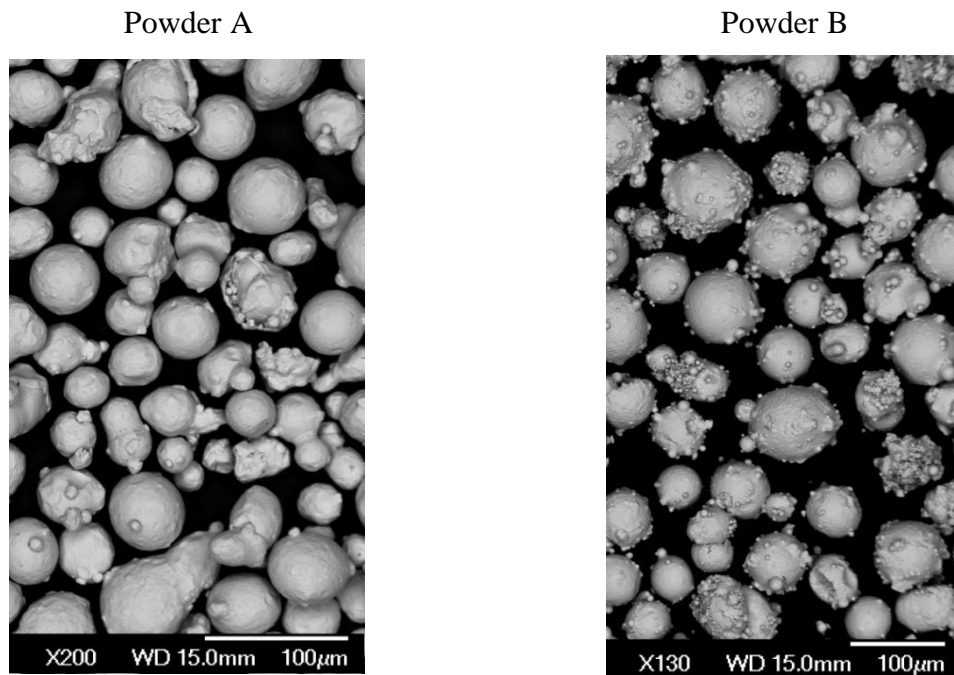
Powder A   Powder B

Figure 8 SEM images showing exemplary particles of each powder (Acceleration voltages: 15,0 kV) [41]

Powders A and B have approximately the same sintered density. It must be noted that the measured apparent density values were higher than the sintered densities of the same powders. The Archimedes densities showed the same ranking, even though the differences were rather small.
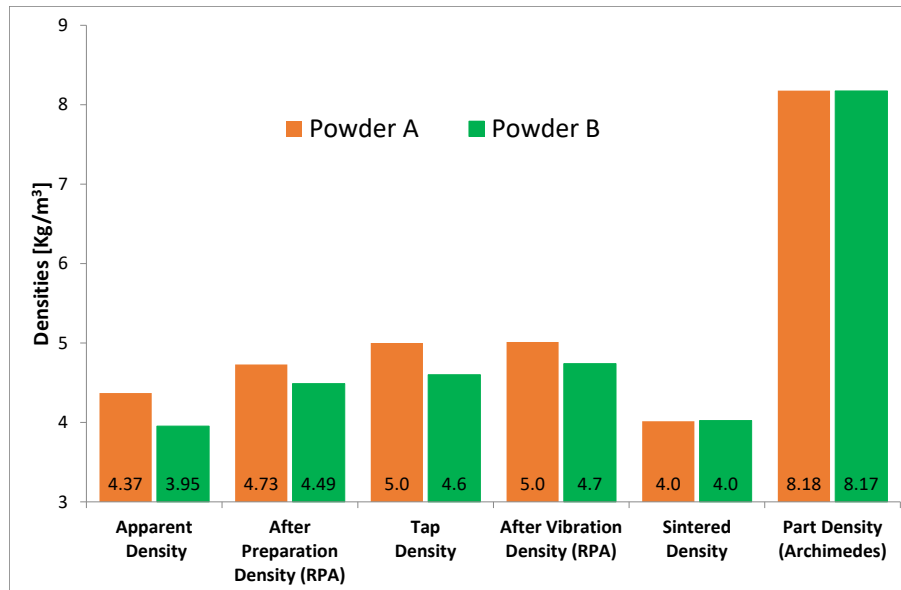
Figure 9 Results of the density evaluations rounded according to the applicable standards [41]

More information for these two powders are descirbed in the [41].

2.2 Laser flash analysis

Laser flash analysis (LFA) has become over the last decades a widely used standard technique to measure the thermal diffusivity of bulk materials under various conditions like different gases, atmospheric pressures, and temperatures. A laser flash apparatus, used to measure material thermal diffusivity, may enable closer replication of in situ powder conditions. Laser flash apparatus was developed based on a study by Parker *et al.* [42].

2.2.1 Laser flash instrument LFA457

The LFA 457 MicroFlash® is the most modern instrument for the determination of the two thermophysical properties, thermal diffusivity and conductivity, in the range from -125°C to 1100°C [43]. This system is used to irradiate the surface of a disc shaped sample of known thickness with a short laser pulse. The time the heat pulse takes to travel through the sample is measured by an infra-red camera directed at the rear face.

Figure 10 illustrates the schematic design of the NETZSCH LFA 457 MicroFlash® (measurement part). Positioned in the base of the device is the head of an Nd:YAG laser. The laser has a pulse length of 330 *μs* and a pulse energy output of up to 15 *J*/pulse. Power is supplied to the laser by a capacitor bank positioned in a separate box. The power output of the laser can be controlled by the software via the voltage level of the capacitor bank and/or via a filter system positioned in the outlet area of the laser system. The laser pulse is deployed through an enlargement optics system which adjusts the beam diameter to the required sample diameters. From the enlargement optics system, the laser pulse is guided via a mirror through a window into the vacuum-tight sample chamber. Inside the sample chamber is an automatic sample changer for up to 3 samples. The samples are positioned in easily user interchangeable sample carriers which can be adjusted to the actual sample dimensions (square samples, disk-shaped samples with various diameters, etc.).

In the NETZSCH Laser flash method, a laser beam is absorbed in a thin layer at the front of the test piece. The temperature distribution inside the test piece depends only on the thermal diffusivity of the material.
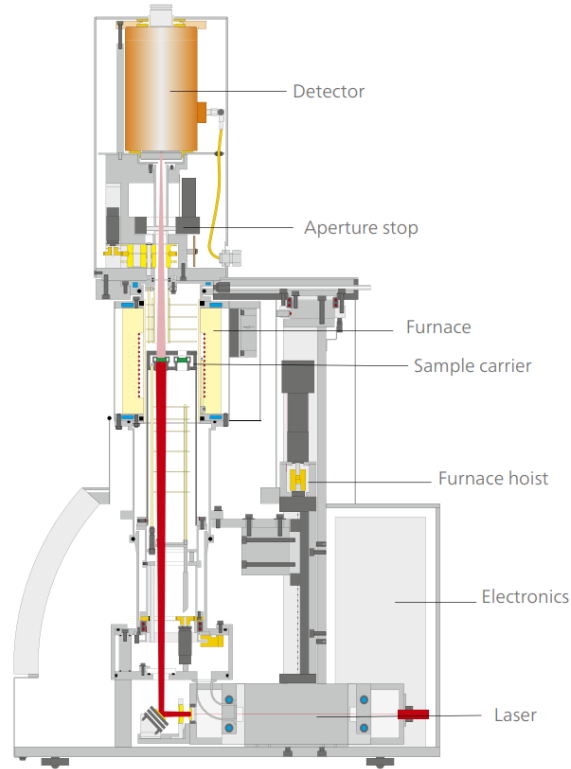
Figure 10 LFA 457 MicroFlash® apparatus (1100°C-Version)

An analytical solution for laser flash thermal diffusivity measurements has been given by Parker *et al*. [42] assuming the following conditions:

1) The duration of laser pulse is negligibly short compared with the characteristic time of heat diffusion.
2) The bottom face of specimen is uniformly heated by a pulse of light.
3) The specimen is adiabatic during the measurement after heating by the pulse of light.
4) The specimen is uniform (in geometry) and homogeneous.
5) The specimen is opaque (nontransparent and non-translucent) to the pulse of light and to thermal radiation.

The thermal conductivities of the solid and powder materials can be calculated through the Laplace relation:

$$k(T) = \alpha(T)\rho(T)C_p(T) \tag{7}$$

where k is the thermal conductivity ($W/(m{\cdot}K)$, α the thermal diffusivity (m^2/s), ρ is the density (kg/m^3) and C_p the specific heat capacity ($J/(kg\ K)$.

The thermal diffusivity value is calculated from the specimen thickness and the time required for the rear face temperature rise to reach a percentage of its maximum value (Figure 12).

$$\alpha = 0.1388 \cdot L^2/t_{1/2} \tag{8}$$

where L is the thickness of the sample and $t_{1/2}$ is the time to reach the half of the maximum temperature.
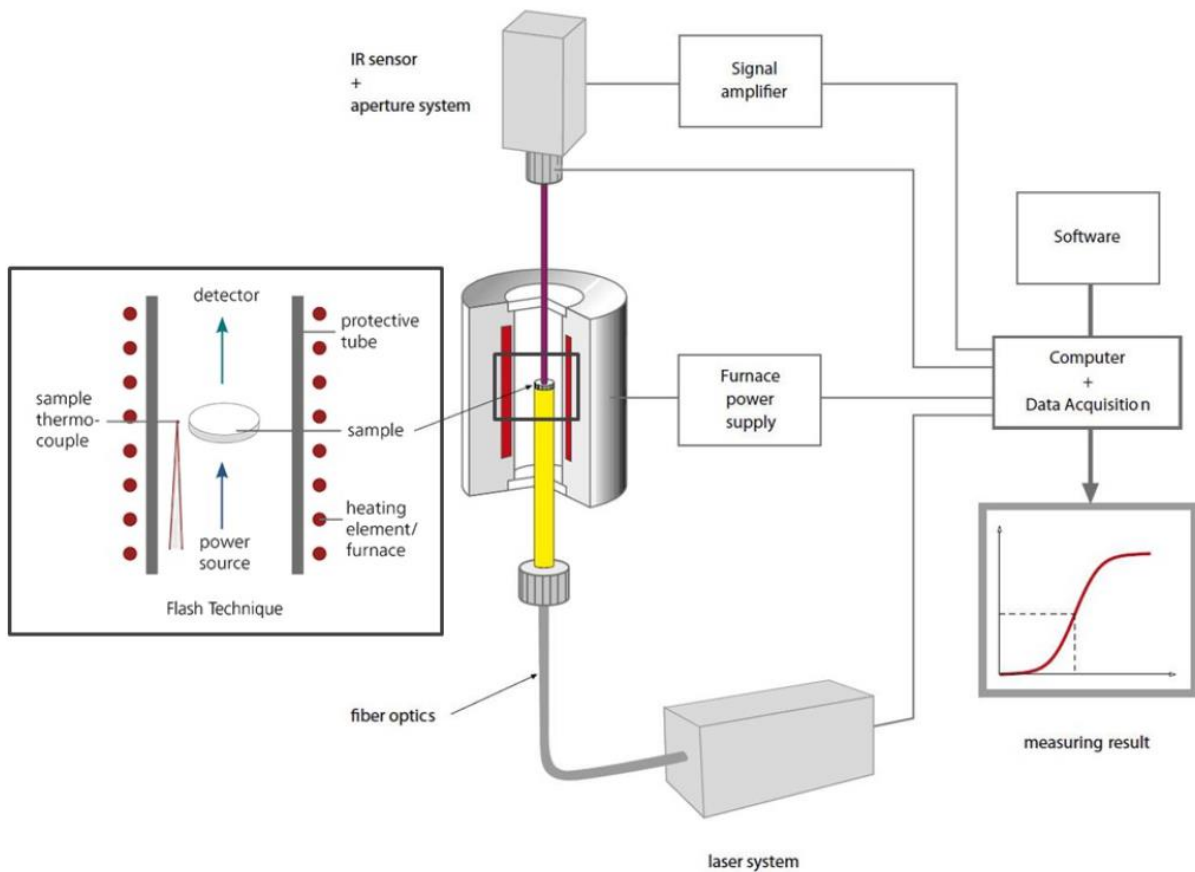
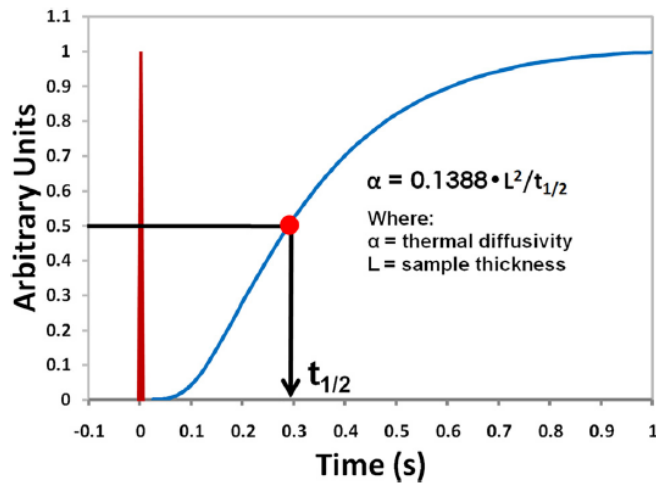*Figure 11 Schematic setup of a typical Laser Flash Apparatus*

$$\alpha = 0.1388 \cdot L^2/t_{1/2}$$

Where:
α = thermal diffusivity
L = sample thickness

Figure 12 Illustration of normalized output curve from measured thermal signals

2.2.2 Measurement procedure

The measurement follows the instructions supplied by Netzsch.

A Netzsch powder crucible was used for the measurement of the selected powder material. The crucible was filled with powder and tapped to allow the powder to settle. Once filled a sapphire lid was placed in contact with the powder and the crucible screwed shut (Figure 13). The

crucible was then placed in the LFA and heated under an argon atmosphere and the diffusivity determined using the Cowen+ pulse correction model.
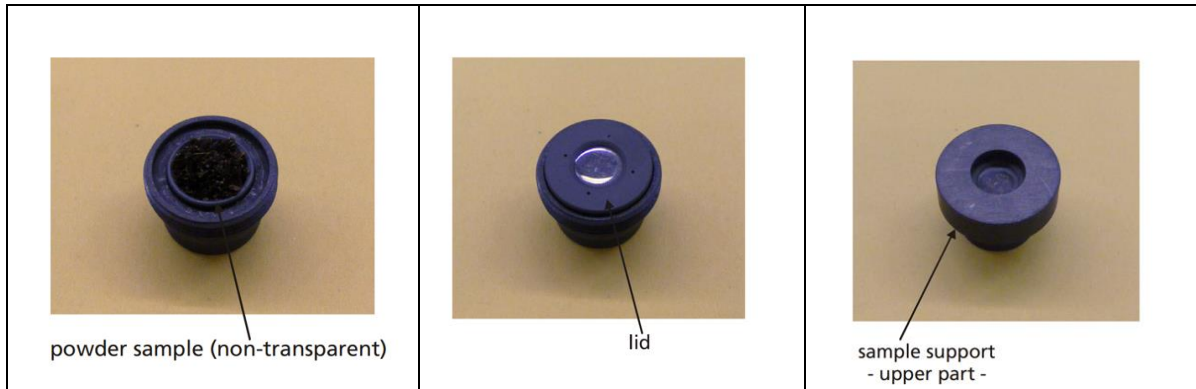
Figure 13 Loading of sample for laser flash test

The thermal diffusivity was measured over a specified temperature ranges with a specified temperature step.

All data are stored a user-defined database for Microsoft Access.

2.2.3 Data analysis

Netzsch Proteus software was used for evaluating measurements from the LFA testing. There are classical models including Parker, Cowan 5, Cowan 10, Azumi, Clark-Taylor [43]. It also includes an improved Cape-Lehman model through consideration of multi-dimensional heat loss and non-linear regression. Figure 14 shows typical data processing using Proteus® software (version 6.0).

The excitation signal used for simulation was a square wave with the duration of 1 *ms* and the peak output of 1 *kW*, giving the total energy of 1 *mJ*. The direct measurement of the laser pulse in a real LFA equipment was also recorded. Its shape is presented in Figure 15.

Each laser shot needs to be evaluated separately. The raw data can therefore be extracted from the Netzsch software as a text file.

Determination of the thermal diffusivity of the graphite layers was performed at three stages:
   a) acquiring the thermal response of specimen to a laser flash excitation with LFA 457;
   b) determination of the effective thermal diffusivity of investigated specimen with the Netzsch Proteus® software;
   c) numerical processing of the collected data with the developed procedure.

For a solid material, the thermal diffusivity and thermal conductivity are determined using equations (2) and (1), respectively.

However, for powder materials, the thermal conductivity cannot be determined directly due to its porous nature. For a powder material, alternative way is used to determine the thermal conductivity. Some intermediate results are prepared for further analysis.
   1) Energy pulse emitted from NETZSCH LFA 457 laser (Figure 15)
   2) Fitting curve of signal from the Netzsch Proteus software (Figure 16)
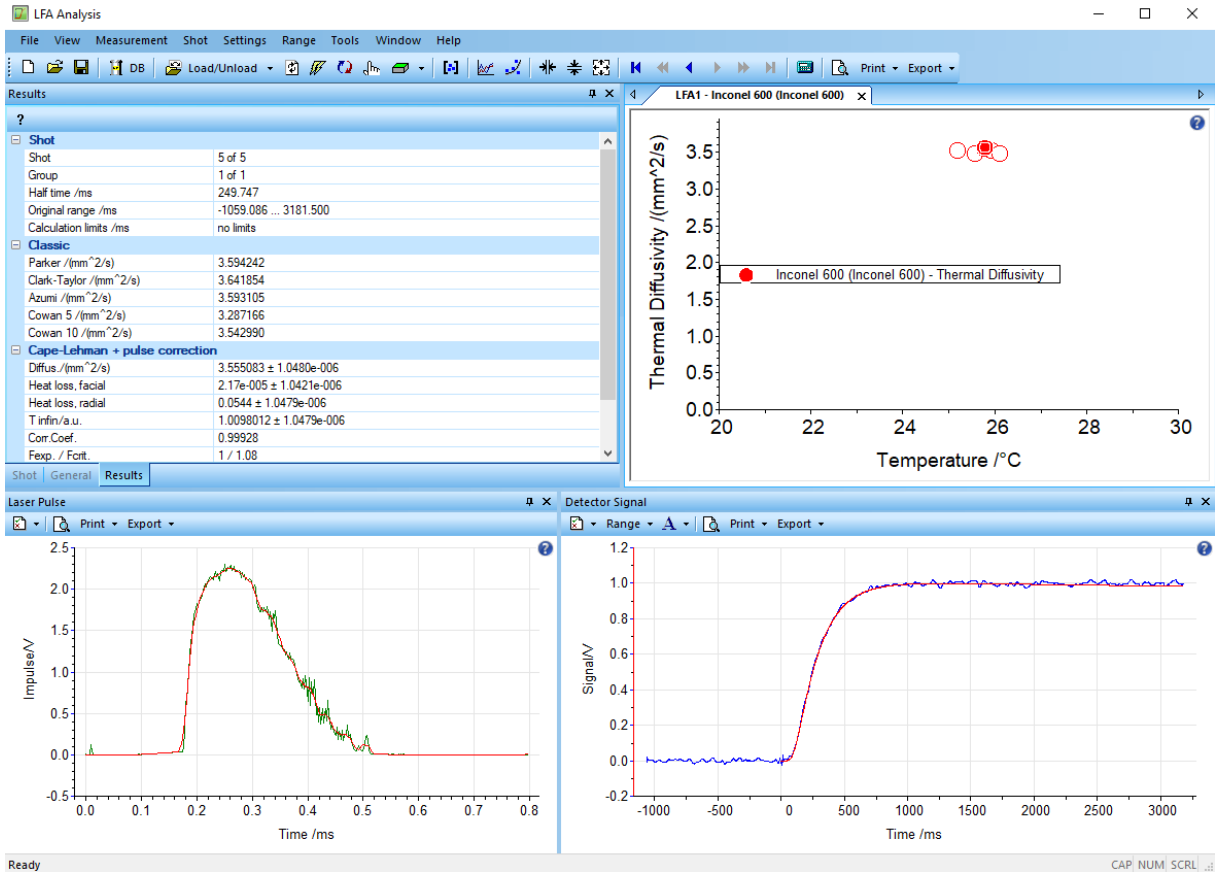   3) Some input data (geometry, heating temperature, etc.)
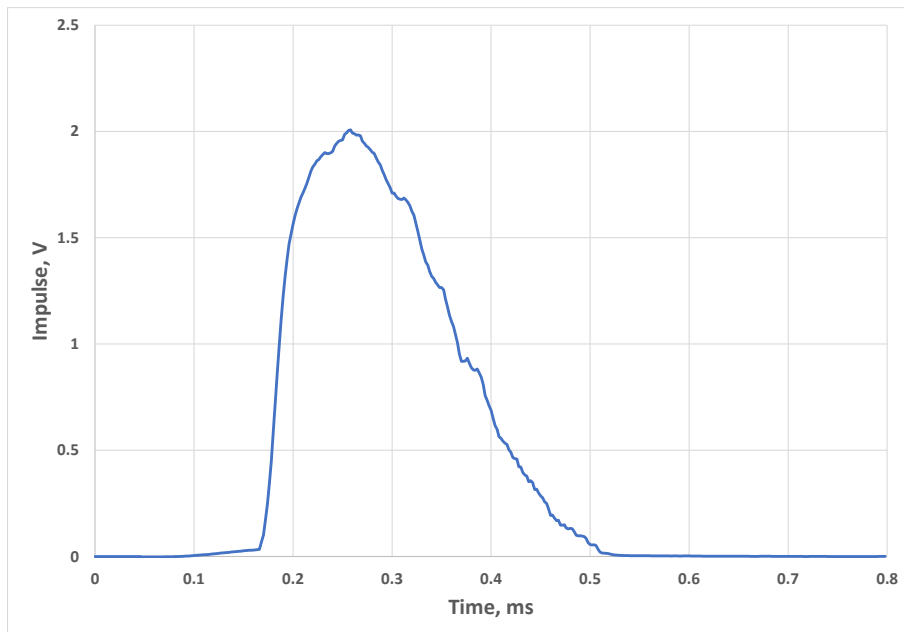
Figure 14 Data analysis using Netzsch Proteus software

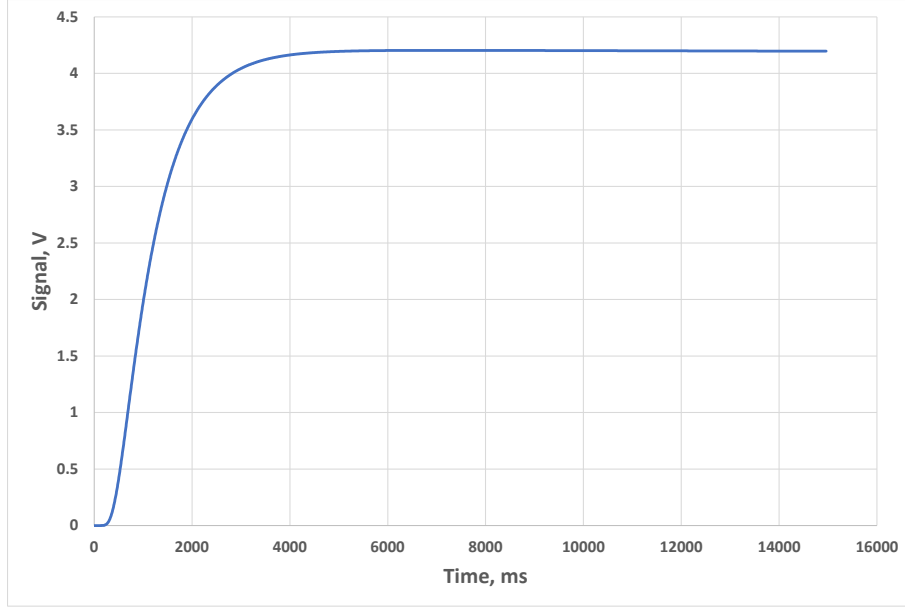*Figure 15 Typical energy pulse emitted from NETZSCH LFA 457 laser*

Figure 16 Fitting curve of signal from the Netzsch Proteus software

2.3 Inverse analysis of thermal property

An inverse problem solution was proposed, including fitting the experimental laser flash data with the results of finite element simulation.

2.3.1 Finite element model

A finite element model was developed using COMSOL Multiphysics software [44].

The heat balance comes from the heat transfer equation.

$$\rho C_p \frac{\partial T}{\partial t} = \nabla \cdot (k \nabla T) + Q \qquad (9)$$

where ρ is density, k thermal conductivity, C_p is specific heat, T temperature, Q is heat source, t time.

Boundary condition (uniform heat source)

$$-\mathbf{n} \cdot \nabla \cdot (k \nabla T) = Q_b \qquad (10)$$

Boundary condition

$$-\mathbf{n} \cdot \nabla \cdot (k \nabla T) = h(T_{amb} - T) \qquad (11)$$

A thin disc sample material of where h is heat transfer coefficient for external natural convection, T_{amb} is the ambient temperature.

The specimen with height H_0 and diameter D_0 is submitted to a laser pulse on one of its faces as shown in Figure 17. The laser pulse delivers a given heat flux from LFA 457 (Figure 11) that is large enough to heat up the opposite face to around 1 K or higher. An axi-symmetry model was employed.

2.3.2 Parameter identification method

The solution of this inverse heat problem is based on the minimization of the ordinary least - square norm. An objective function can be defined as a square error between the measured and calculated temperatures:

16

$$\Phi = \sum_{i=1}^{n}(T_i^m - T_i^c(\boldsymbol{P}))^2 \tag{12}$$

where: Φ is the sum of squares error, $\boldsymbol{P}$ the vector of unknown parameters, $T_i^c(\boldsymbol{P})$ the calculated temperature at time t_i, T_i^m the "measured" temperature at time t_i.
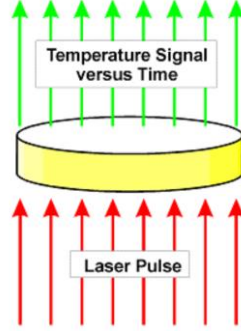

Figure 17 The schematic of LFA measurement

The vector of the unknown parameters of the model is:

$\boldsymbol{P} = [k, \rho, q, h]$ \hfill (13)

SNOPT (Sparse Nonlinear OPTimizer) was used to find the least square minimum between the experimental thermograms and the model thermograms, which is a built-in functionality in COMSOL software package for solving large-scale nonlinear optimization problems [44]. The SNOPT method allows to set bounds on the unknown parameters.

2.3.3 Parameter identification procedure

For a LFA 457 test, the parameter identification can be done by using the prepared COMSOL finite element model, which is implemented by following procedure:

1) Input heat source data (pulse – time signal) from LFA 457 testing;
2) Input measured temperature data (temperature signal – time) from LFA 457 testing;
3) Input initial temperature value;
4) Input heat capacity calculated by Thermo-Calc for the specified heating temperature;
5) Set initial guesses of parameters;
6) Execute finite element computation;
7) Output results.

In the current study, four unknown variables are selected as identification parameters: powder thermal conductivity (k), powder bed density (ρ), heat source factor and heat transfer coefficient. The developed procedure was proven to be effective and efficient.

2.3.4 Fitted results

A typical temperature contour at nominal temperature 600 °C after 50 seconds is shown in Figure 18. A typical simulated (FEM) temperature vs. time with comparison with experiment (LFA) is plotted in Figure 19. A very good fitting was obtained.
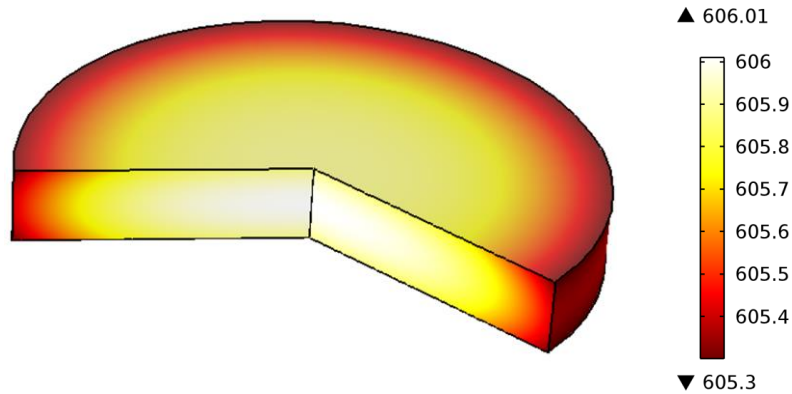
Figure 18 Simulated temperature contour (unit: °C) at nominal temperature 600 °C after 50 seconds.
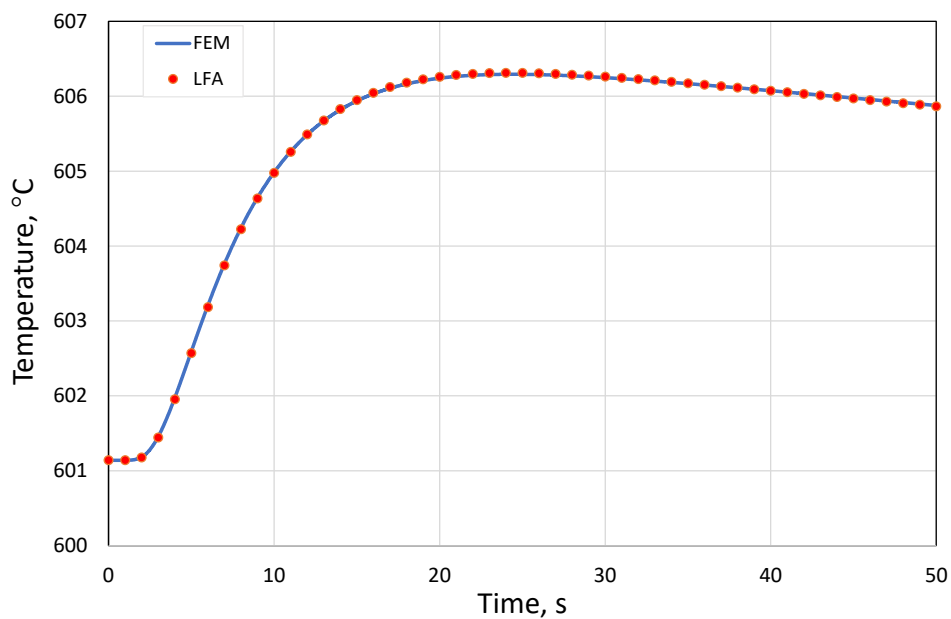

Figure 19 Typical simulated (FEM) temperature vs. time with comparison with experiment (LFA) at nominal temperature 600 °C

The LFA measurements for the selected powders were performed with the temperatures ranging from 100 to 1100 °C. The resulting thermal conductivities vs. temperature for the two powders are presented in Figure 20. It is found that the thermal conductivity of both powders increases with increasing temperature for the investigated temperature range, giving larger difference at higher temperatures between the two powders. In contrast, the relative densities for the two powders are almost same at the sintering temperature (around 1000 °C, see Fig. 9), which implies that the thermal conductivity is more probably influenced by changes to the morphology of powder at higher temperatures.

The thermal diffusivity values measured by the laser flash (directly output from the LFA 457 system using the Cowen + pulse correction model) were compared with the simulated data at different temperatures and summarized in Figure 21, indicating that there is a reasonable agreement between the two. This confirms that the fitted thermal conductivities are also reasonable.

The thermal conductivity of Argon gas was calculated by using open-source code "Cantera". Cantera [45] is a suite of object-oriented software tools for problems involving chemical

kinetics, thermodynamics, and/or transport processes. The curve of thermal conductivity over full range of temperature for argon is shown in Figure 22 giving following fitting equation:

$$k_{A_r} = -6.766459 \cdot 10^{-15} T^4 + 3.278052 \cdot 10^{-11} T^3 - 6.185494 \cdot 10^{-8} T^2 + 8.077229 \cdot 10^{-5} T - 1.657175 \cdot 10^{-3}$$
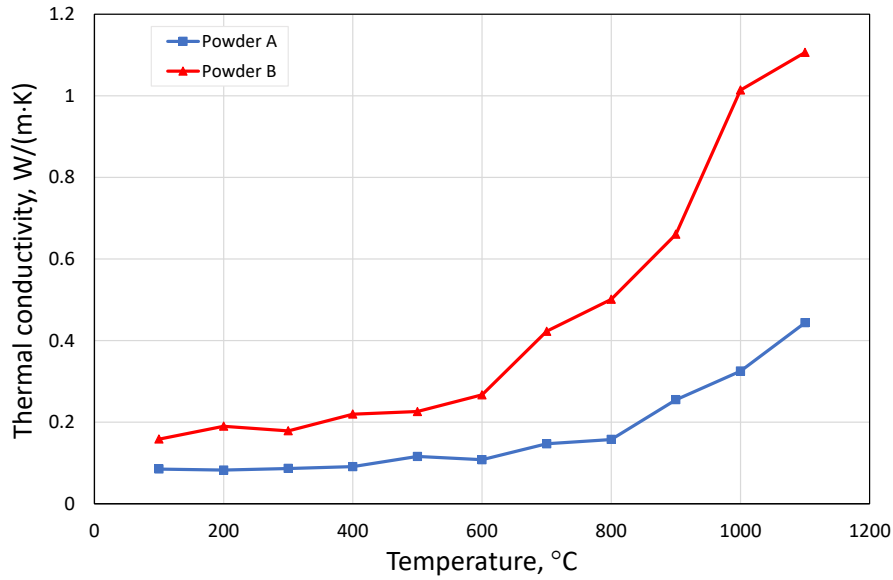

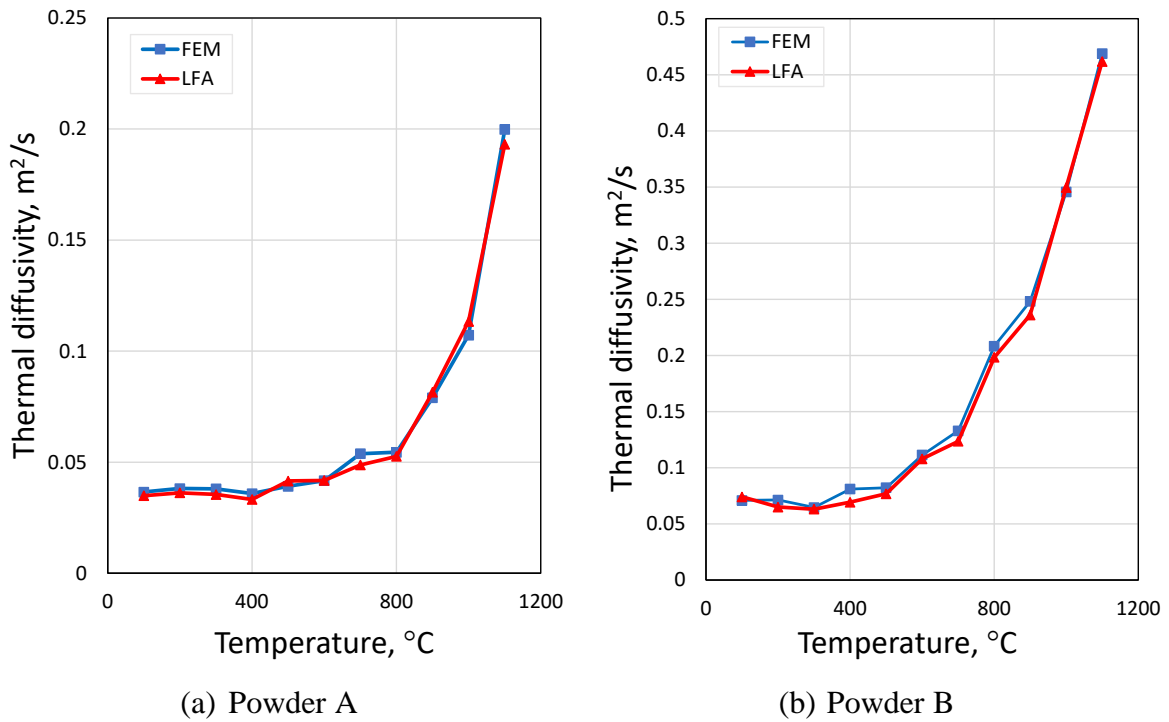*Figure 20 Resulted thermal conductivities at different temperatures.*

(a) Powder A

(b) Powder B

Figure 21 Comparison of measured and simulated thermal diffusivities over temperature for the powders: (a) Powder A; (b) Powder B.

The chart shows the equation:
$$y = -6.766459E{-}15x^4 + 3.278052E{-}11x^3 - 6.185494E{-}08x^2 + 8.077229E{-}05x - 1.657175E{-}03$$
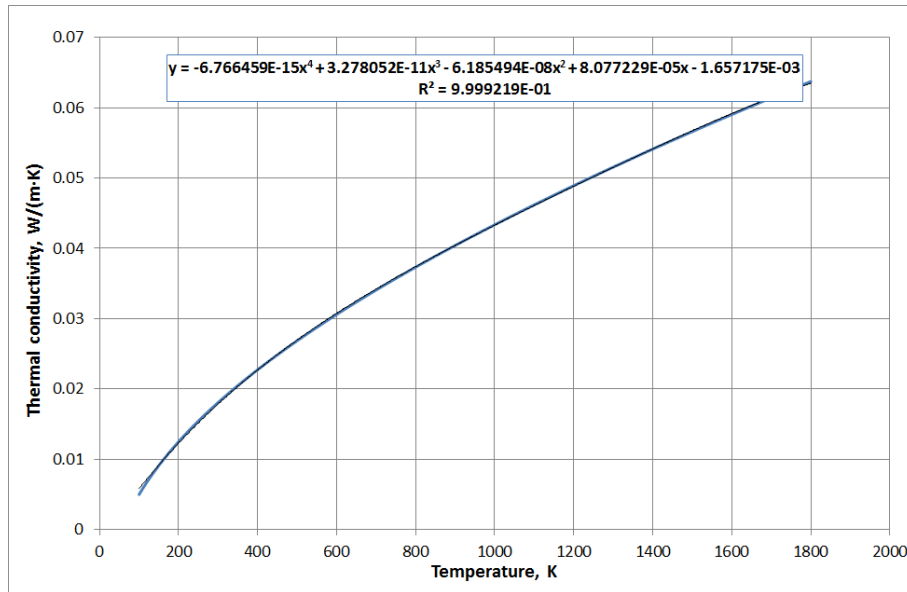$$R^2 = 9.999219E{-}01$$

Figure 22 Thermal conductivity of Argon gas over temperature

2.4 Thermodynamic analysis and calculations of the selected Alloy by CALPHAD method

The deviations are linked to formation of minor phases in the computation since the computation is always performed for equilibrium states.

The CALPHAD method is used to find the thermodynamic properties of different materials system. The CALPHAD method was established as tool for phase equilibria of different multicomponent systems and for treating thermodynamics. Thermo-Calc was used in this project.

Temperature-dependent data can be calculated using Thermo-Calc.

1) Phase fractions vs. temperature;
2) Thermal properties, like enthalpy, heat capacity, density, etc;
3) Liquidus and solidus temperatures.

Fig. 23 shows the phase fraction vs. temperature for IN 718 with equilibrium calculation using Thermo-Calc. It is used only for reference since the AM process has a quick large differnces compared to equilibrium process.

The calculated density and specific heat capacity over temperature are shown in Fig. 24. There might be some deviations due to the formation of minor phases in the computation since the computation is performed for almost equilibrium states.
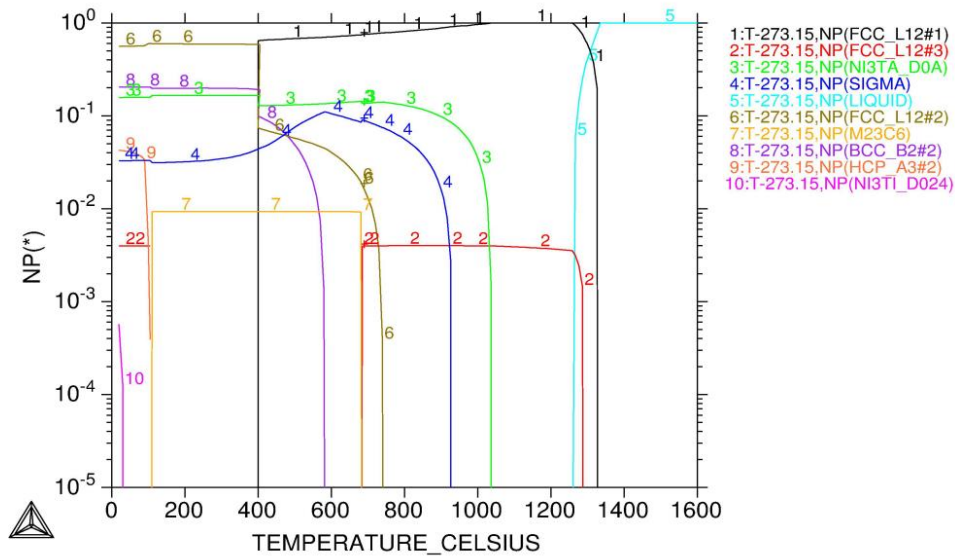
a) Powder A
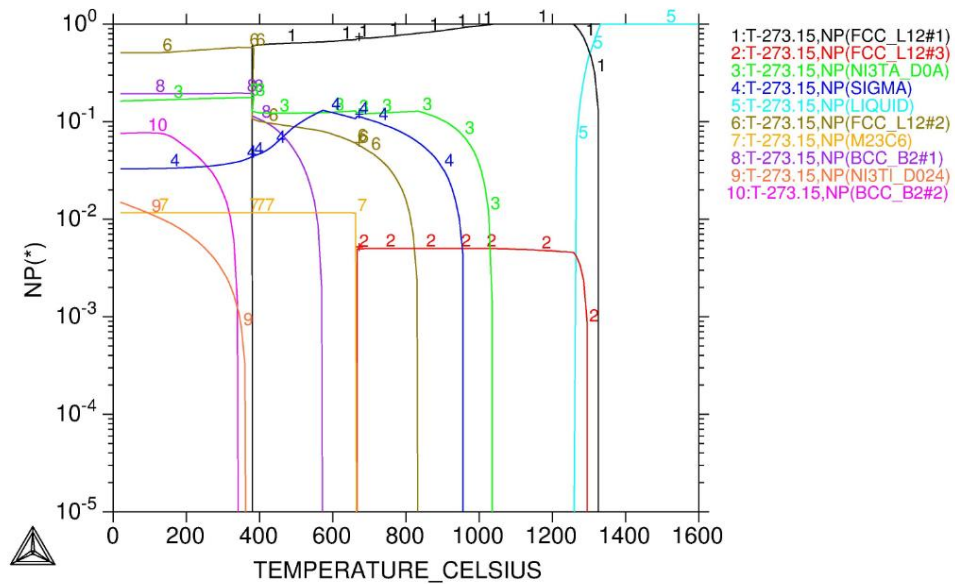
b) Powder B

Figure 23 Phase fraction vs. temperature for IN 718 with equilibrium calculation using Thermo-Calc (2020b)
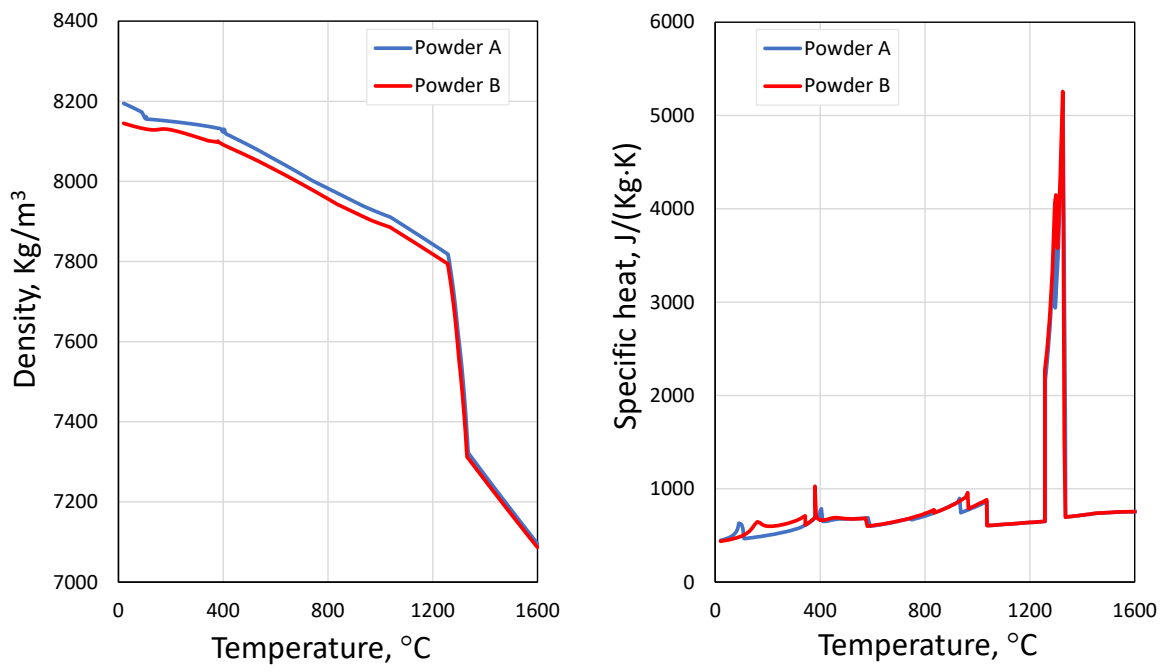
Figure 24 Density and specific heat capacity over temperature using Thermo-Calc (2020b)

3 Analytical solution of thermal model

The aim of analytical solution of thermal model is to predict three main quantities:

    1) the temperature distribution;

    2) temperature history of any tracing point;

    3) the melt pool size (length, width and depth).

3.1 Transient analytical heat conduction model for temperature - dependent properties

The governing equation for conduction heat flow is written as

$$\rho C_p \frac{\partial T(x,y,z,t)}{\partial t} = \nabla \cdot (k \nabla^2 T(x,y,z,t) + Q_V \tag{14}$$

where k is the thermal conductivity, c_p the specific heat capacity, ρ the density, t the time, T the temperature, and Q_V the volumetric heat source term expressed as energy density per unit volume. $T(x, y, z, t)$ is abbreviated to T in the remaining of this report.

Assuming none of its constituent quantities are functions of temperature, enables the simplification of equation (9) to the well-known form of the heat conduction equation.

$$\frac{\partial T}{\partial t} = \alpha \nabla^2 T \tag{15}$$

where α is the thermal diffusivity ($\alpha = k/(\rho\, c_p)$).

Equation (14) or (15) can be solved based on the following assumptions:

    1) The material is considered homogeneous and isotropic.

    2) The material has constant material properties.

    3) No heat loss from the surface by radiation and convection are not considered.

The well-known Rosenthal equation describes the three-dimensional, steady state temperature field for a point heat source moving in the x-direction:

$$T(t) = T_0 + \frac{q}{2\pi k R} \cdot exp\left\{ -\frac{v(x+R)}{2\alpha} \right\} \tag{16}$$

where T_0 is the initial temperature, q the absorbed power, v the scan speed. The distance R from the beam location to the interest point is

$$R = \sqrt{x^2 + y^2 + z^2} \tag{17}$$

where the coordinates (x, y, z) are written relative to the position of the beam.

The Rosenthal equation is often utilized to examine cases where the area of heat application (*e.g.*, laser spot size) is much smaller than the dimensions of features of interest. It is noticed that the solution is singular as $R \rightarrow 0$, because of the infinitely concentrated heat source.

A Gaussian distributed heat source is more appropriate to be applied to AM. There are two kinds of Gaussian heat sources which are most used for AM modeling and simulation. The heat sources and the corresponding temperature solutions are presented as below.

3.1.1 Planar Gaussian heat source

A moving planar Gaussian distributed heat source as shown in Figure 25 has following form

$$Q(x,y) = \frac{\eta P}{2\pi \sigma^2} \exp\left(-\frac{x^2+y^2}{2\sigma^2}\right) \tag{18}$$

where P is the beam power, η the absorptivity, σ is the standard deviation of the Gaussian beam. Based on the plan Gaussian heat source (18) and heat transfer equation (9), an analytical solution of temperature field is derived by Eagar and Tsai [46] using the Green's function method

$$T(t) = T_0 + \frac{2\eta P}{\rho c_p \pi \sqrt{\pi}} \int_0^t \frac{1}{4\alpha\tau+2\sigma^2} \cdot \frac{1}{\sqrt{4\alpha\tau}} \cdot exp\left\{-\frac{(x-v_x t')^2+y^2}{4\alpha\tau+2\sigma^2} - \frac{z^2}{4\alpha\tau}\right\} dt' \qquad (19)$$

where t' is an integration variable for time, $\tau = t - t'$ is the time available for conduction from the transient location of the heat source at time t' to the location of the point of interest at time t.
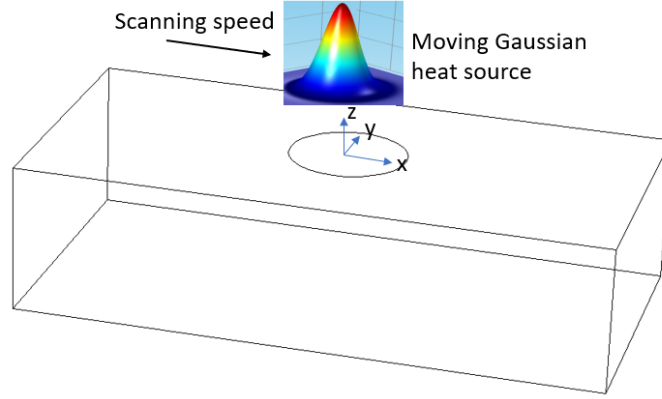

Figure 25 A moving Gaussian heat source heats on the semi-infinite substrate

3.1.2 Volumetric Gaussian heat source

$$Q(x, y, z) = \frac{6\sqrt{3}\eta P}{\pi\sqrt{\pi}r_b^2 d_p} \exp\left(-\frac{3(x^2+y^2)}{r_b^2} - \frac{3z^2}{d_p^2}\right) \qquad (20)$$

where r_b radius of beam, d_p penetration depth.

Using the separation of variables, the closed form solution of the transient temperature field can be expressed as [47]

$$T(t) = T_0 + \frac{6\sqrt{3}\eta P}{\rho c_p \pi \sqrt{\pi}} \int_0^t \frac{1}{12\alpha\tau+\sigma^2} \cdot \frac{1}{\sqrt{12\alpha\tau}} \cdot exp\left\{-\frac{3[(x-v_x t')^2+y^2]}{12\alpha\tau+\sigma^2} - \frac{3z^2}{12\alpha\tau}\right\} dt' \qquad (21)$$

where t' is an integration variable for time, $\tau = t - t'$ is the time available for conduction from the transient location of the heat source at time t' to the location of the point of interest at time t.

The material properties are expressed as functions of temperature $k(T)$, $c_p(T)$, $\rho(T)$, and $\alpha(T)$. Two quantities $\Psi(t)$ and $\Phi(t, T)$ are denoted as

$$\Psi(t) = 12\alpha(T)\tau + \sigma_i^2 \qquad \text{for } i = x, y, z \qquad (22)$$

$$\Phi(t, T) = \frac{6\sqrt{3}\eta P(t)}{\rho(T)c_p(T)\pi\sqrt{\pi}} \qquad (23)$$

The positions relative to the heat source center is described as

$$\bar{x}_q(t) = x - x_q(t) \qquad (24)$$

$$\bar{y}_q(t) = x - y_q(t) \qquad (25)$$

$$\bar{z}_q(t) = z - z_b{}^t \qquad (26)$$

Equation (14) with consideration of variable material properties is rewritten as

$$\hat{T}(t) = T_0 + \Phi(t,T) \int_0^t \frac{1}{\sqrt{\Psi_x \Psi_y \Psi_z}} \cdot exp\left\{ -\frac{3\bar{x}_q(\tau)^2}{\Psi_x} - \frac{3\bar{y}_q(\tau)^2}{\Psi_y} - \frac{3\bar{z}_q(\tau)^2}{\Psi_z} \right\} dt' \qquad (27)$$

Flow simulation in the melt pool is extremely computationally. An alternative way is to enlarge the thermal conductivity to consider the thermocapillary convection (Marangoni flow) effect on the thermal field, resulting in reasonable accuracy.

3.2 Powder bed properties and liquidus temperature

The PBF process uses a beam (laser or electron) as the heat source to selectively melt the metallic powder particles of the layer according to the CAD model, thereby forming a pool of liquid material. The material then resolidifies after a period of cooling. Due to the small interaction volume, the heating and cooling rates are very high. The liquid begins to solidify for a very short amount of time after the beam is removed. There are three states of the material: powder, molten and re-solidified for a single phase (Figure 26).
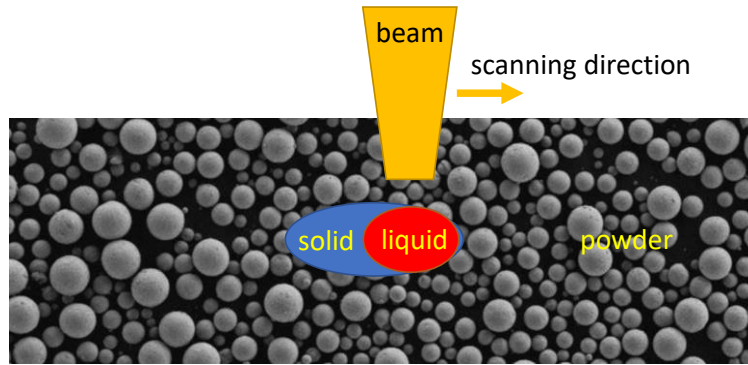

Figure 26 Schematic view of the PBF process with respect to materials states: powder, liquid and re-solidified material

Both numerical and analytical calculations for AM processes require thermophysical properties of alloys such as thermal conductivity, specific heat, density and liquidus temperature. If these properties are assumed to be constant, it will lead to incorrect results since they are temperature - dependent.

The powder bed is often treated as a homogeneous medium with effective thermophysical properties to reduce the computational costs.

As the powder-bed is regarded as a mixture of solid powders and gas (for example, argon is used in LB-PBF) phases. A mixture rule is used for calculating density and specific heat of powder bed in AM.

3.2.1 Density

The density of powder bed is written as

$$\rho_{powder} = (1-\varphi)\rho_{solid} + \varphi\rho_{gas} \qquad (28)$$

where φ is the porosity of powder bed, ρ_{solid} is the density of bulk material, and ρ_{gas} is the density of the gas. If the density of the used gas is relatively very low compared with that of solid, it can be omitted.

The effective density of powder is calculated based on the temperature region:

$$\bar{\rho}_{powder} = \begin{cases} \rho_{powder}(T) & T \leq T_S \\ \frac{\rho_{liquid}(T_L) - \rho_{powder}(T_S)}{T_L - T_S} \cdot (T - T_S) + \rho_{powder}(T_S) & T_S < T < T_L \\ \rho_{liquid}(T) & T \geq T_L \end{cases} \tag{29}$$

where T_S and T_L are solidus and liquidus temperatures, respectively.

3.2.2   Specific heat

The specific heat of powder bed is written as

$$Cp_{powder} = \frac{(1-\varphi)\rho_{solid}Cp_{solid} + \varphi\rho_{gas}Cp_{gas}}{\rho_{powder}} \tag{30}$$

where Cp_{powder}, Cp_{solid} and Cp_{gas} are the specific heat of the powder bed, bulk material and gas, respectively. The specific heat of the powder bed is approximately regarded as that of solid material if the density of the gas is very low.

The melting, solidification and solid-state phase transformation take place during the AM process. There are two alternative methods to treat the heat capacity:

1)   Use the calculated effective heat capacity based on latent heat and liquid fraction.

An effective heat capacity ($\bar{C}_p$) is expressed as

$$\bar{C}_p = C_p(T) + L_f \frac{\partial f}{\partial T} \tag{31}$$

$$f = \begin{cases} 0 & T \leq T_S \\ \frac{T - T_S}{T_L - T_S} & T_S < T < T_L \\ 1 & T \geq T_L \end{cases} \tag{32}$$

where $C_p(T)$ is temperature dependent specific heat, L_f the latent heat of fusion, f liquid fraction, T_s solidus temperature, T_L liquidus temperature.

2)   Directly use the $Cp - T$ curve calculated from the calculation by CALPHAD.

3.2.3   Thermal conductivity

The thermal conductivity of powder bed is written as

$$k_{powder} = \begin{cases} k_{powder}(T) & T \leq T_S \\ \frac{k_{liquid}(T_L) - k_{powder}(T_S)}{T_L - T_S} \cdot (T - T_S) + k_{powder}(T_S) & T_S < T < T_L \\ k_{liquid}(T) & T \geq T_L \end{cases} \tag{33}$$

3.2.4   Liquidus

The liquidus temperature is obtained in two ways:
   1) Literature or book
   2) CALPHAD – based computational software (like Thermo-Calc, JMatPro)

For a typical AlSi10Mg (10%Si, 0.3%Mg, 0.3%Fe, 0.08%Cu), the solidification process is calculated by using Thermo-Calc. The liquidus temperature is about 594 °C.

3.3   Temperature calculation procedure

Based on the models described in the section 3.1, the temperature history at specified location can be calculated. Fig. 27 shows the flow chart for calculating the temperature history at specified location in the build domain.
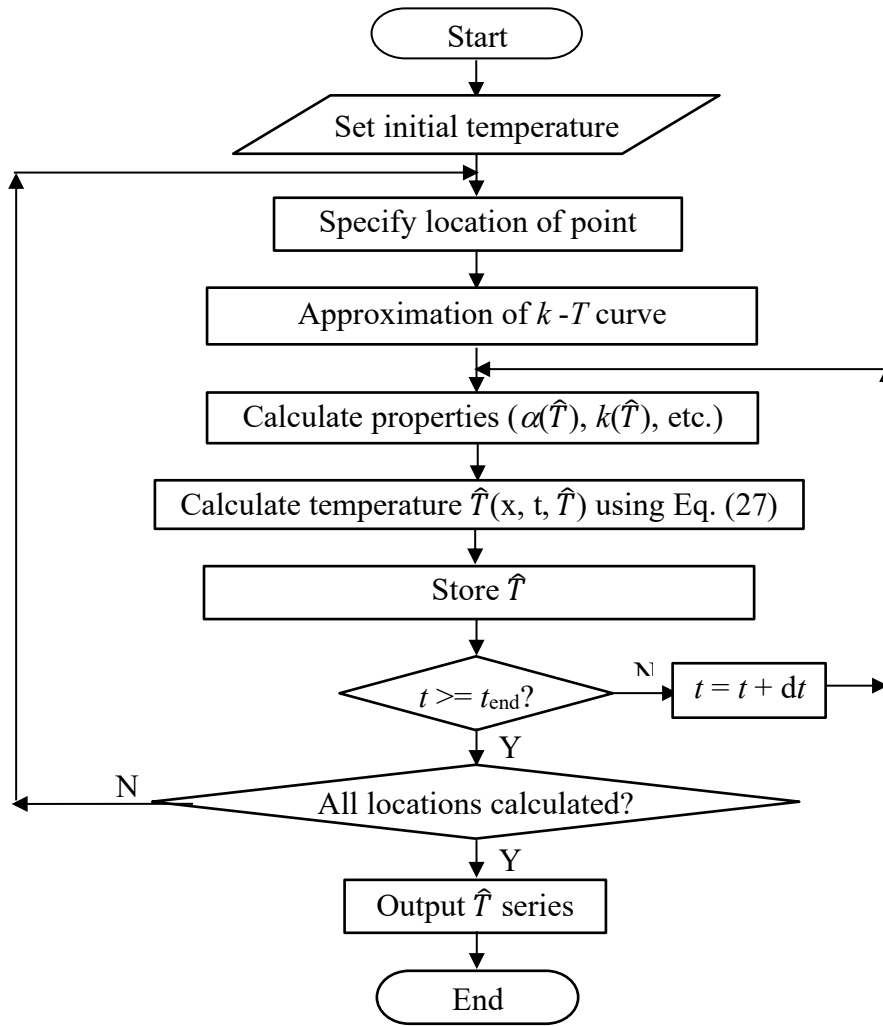
Figure 27 Flow chart to calculate temperature history.

Compared with traditional numerical methods for solving heat transfer problem, the advantage of this semi-analytical method is that the thermal history of each point is independent of all other points, and each time is independent of all other times. Therefore, very short calculation time is needed if it is only interested in temperature histories for certain specified points. In addition, this independence allows the simulation to be easily parallelized to further improve the calculation time for temperature field computation.

Special treatment on thermal conductivity:

Using equation (27) and new developed segment-wise integration procedure can result a reasonable approximation of temperature for solid material with temperature – dependent properties. However, for a powder material, the thermal properties change drastically with temperature, resulting in a deviation for the calculated temperature. Therefore, a special treatment for thermal conductions near liquidus temperature is implemented according to the following steps:

1) Calculating average value of two factors (w_k and w_α)

$$\bar{w} = (w_k + w_\alpha)/2 \tag{34}$$

$$w_k = LN\left(\frac{\bar{k}_{sol}}{k_{liq}}\right)$$ (35)

$\bar{k}_{sol}$ average thermal conductivity over a range of temperature points less than liquidus temperature. k_{liq} conductivity at liquidus temperature.

$$w_\alpha = LN\left(\frac{\bar{\alpha}_{sol}}{\alpha_{liq}}\right)$$ (36)

$\bar{\alpha}_{sol}$ average thermal diffusivity over a range of temperature points less than liquidus temperature. α_{liq} diffusivity at liquidus temperature.

2) k_{mod} is calculated until the following condition is satisfied:

$$\bar{k}_{mod}/\bar{k}_{sol} \geq \bar{w}$$ (37)

where k_{mod} and σ are expressed as

$$k_{mod} = (1-\sigma)k_{sol} + \sigma k_{liq}$$ (38)

$$\sigma = \frac{1}{1+\exp\left(-(T-T_{mid})/p\right)}$$ (39)

The exponential transition approach (equations 38 and 39) used here allows one to create a mathematically smooth function tween the data segments k_{sol} and k_{liq}.

This treatment is necessary for the case of LB-PBF.

3.4   Validation of analytical model with FEM (COMSOL)

To validate the analytical model and its calculation procedure, a three-dimensional transient finite element model (Figure 28) was created using COMSOL, having a domain of size (2 mm length (*l*) by 1.5 mm width (*w*) by 0.2 mm thickness (*h*)). A laser scanning path of a single track in which laser moves along the x-axis from position *A* ($x = 0.5$ mm) to position *B* ($x = 1.5$ mm) was designed to support the semi-infinite assumption. The planar Gaussian distributed heat source as expressed in equation (18) was used for both FEM and analytical method. The equation (27) was used to calculate temperature field and temperature histories in the analytical method (refer to Figure 27).

LB-PBF process of AlSi10Mg was selected for validation. The effective temperature-dependent thermal conductivities of both solid and powder AlSi10Mg are shown in Figure 29 [18], in which only solid data are utilized for validation. The calculated temperature-dependent specific heat of AlSi10Mg using CALPHAD method is shown in Fig. 30a. The temperature-dependent density heat for solid AlSi10Mg was calculated using CALPHAD method and then the corresponding values for powder are calculated using equations (28) and (29) which are shown in Fig. 30b.

The materials properties and process parameters are listed in Table 6.

Table 6 Materials properties and process parameters for LB-PBF of solid AlSi10Mg

Thermal conductivity (W/m·K)	See Figure 29 (solid)
Specific heat (J/kg·K)	See Figure 29a
Density (kg/m^3)	See Figure 29b (solid)
Liquidus temperature (°C)	594
Initial temperature (°C)	20
Laser velocity (m/s)	2.0
Laser power (W)	100
spot size (µm)	80
Absorption	0.6
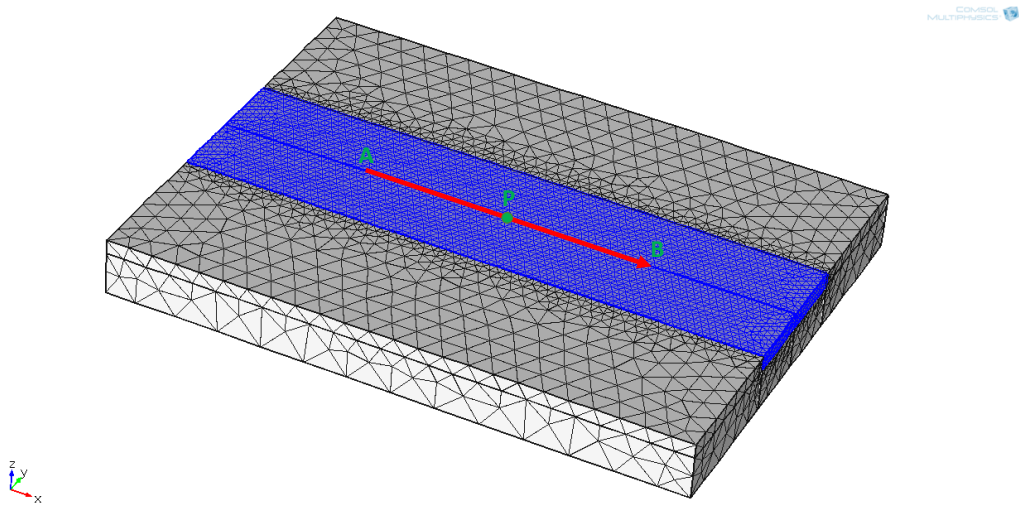
Figure 28 Finite element mesh using COMSOL (length: 2 mm, width: 1.5 mm, height: 0.2 mm)
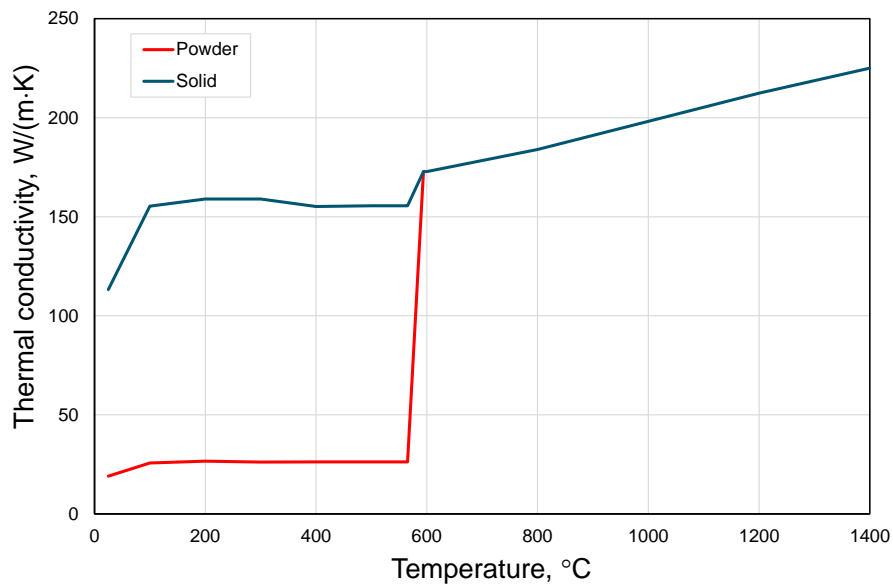
Figure 29 Temperature-dependent thermal conductivity of solid AlSI10Mg [18]
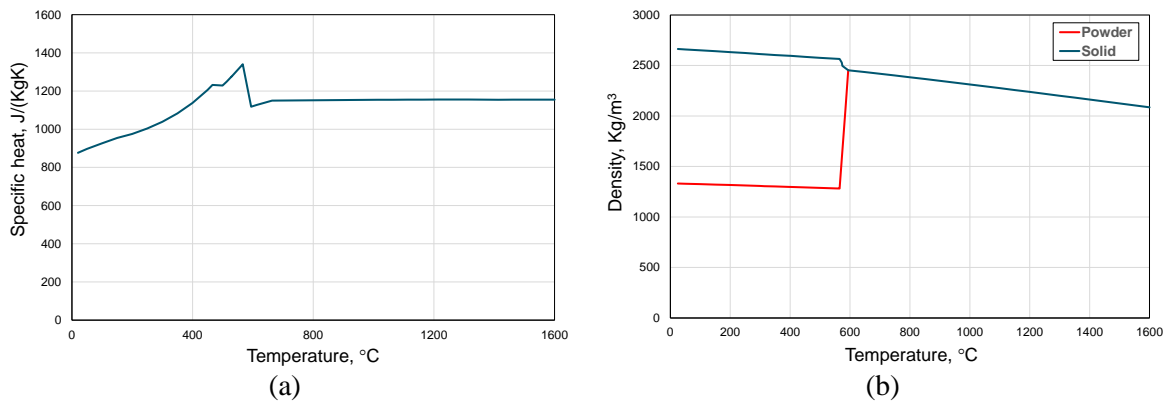
Figure 30 Calculated temperature-dependent thermal properties of AlSi10Mg powder using CALPHAD method: specific heat capacity (a) and density (b)

The top view of temperature contours at the time moment ($t = l_{AB}/2v$, position P) that the laser beam moves to a half-track length for selective laser melting of solid AlSi10Mg predicted by using analytical method (top) and FEM (bottom) is shown in Figure 31. The melt pool boundary is indicated by the solid black line. It was demonstrated that the analytical method accurately predicts temperature distributions approximating those calculated by existing FEA method. Furthermore, a very close agreement between the analytical model and the FEM model regarding the melt pool shape and dimensions is seen from the two figures (Figure 32).
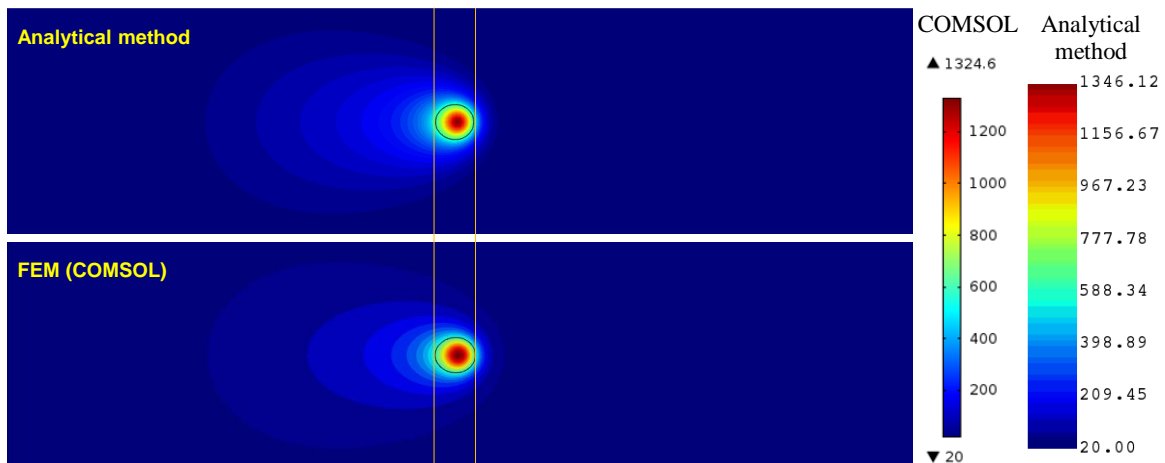

Figure 31 Top view of temperature contours at the time moment ($t = l_{AB}/2v$) that the laser beam moves to a half-track length for selective laser melting of solid AlSi10Mg predicted by using analytical method (top) and FEM (bottom). The melt pool boundary is indicated by the solid black line.
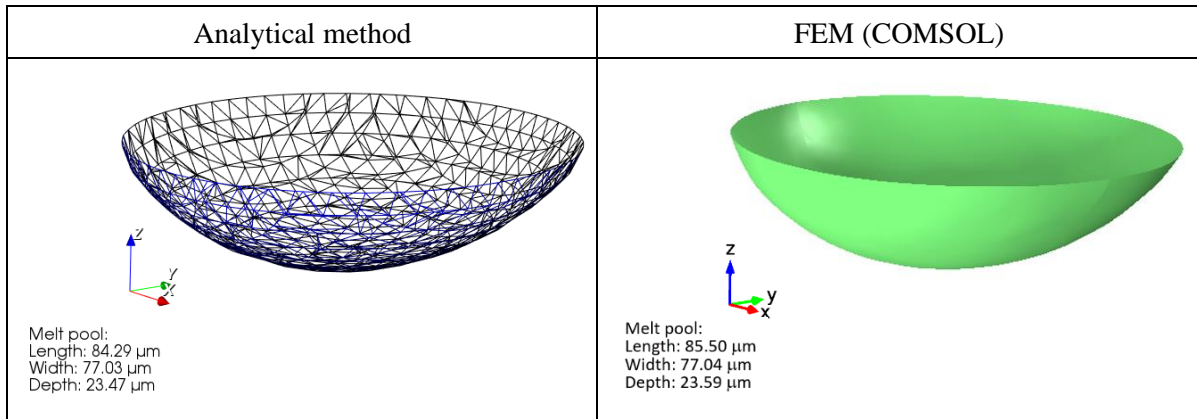
30

Analytical method	FEM (COMSOL)
Melt pool: Length: 84.29 µm Width: 77.03 µm Depth: 23.47 µm	Melt pool: Length: 85.50 µm Width: 77.04 µm Depth: 23.59 µm

Figure 32 Melt pool profile comparison between the analytical method and FEM (COMSOL) for selective laser melting of powder AlSi10Mg

Figure 31 shows temperature profile comparison between analytical method and FEM at section $y = w/2$ and at time moment ($t = l_{AB}/2v$) on top surface. Figure 34 shows temperature profile comparison between analytical method and FEM at section $x = l/2$ and at time moment ($t = l_{AB}/2v$) on top surface. It is seen that the temperature profile modeled by the analytical method matches the FEM result within 2%. In addition, the length and width of melt pool based on the intersection between profile line and liquidus line gives more precise results from the two methods.
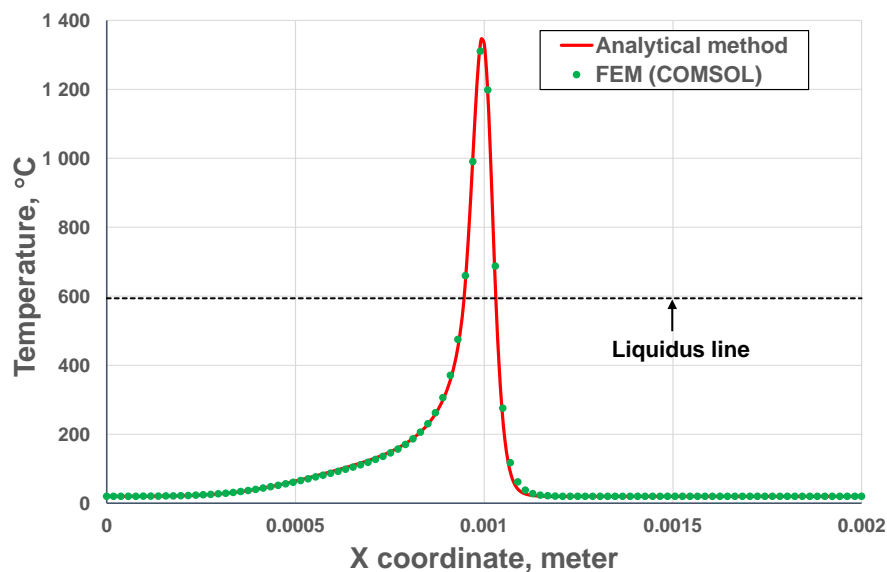

Figure 33 Temperature profile comparison between analytical method and FEM for LB-PBF of powder AlSi10Mg for section at y = w/2 and at time moment (t = l_{AB}/2v) on top surface
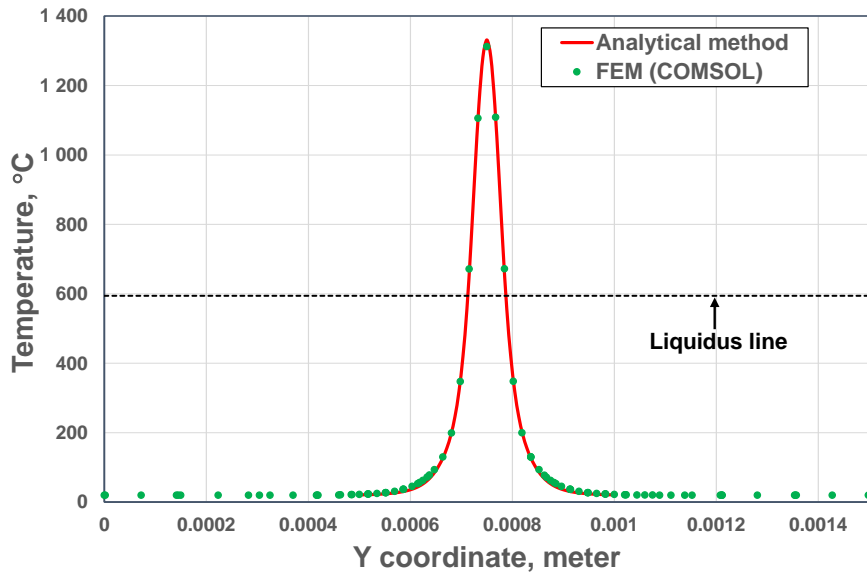
31

Figure 34 Temperature profile comparison between analytical method and FEM for LB-PBF of powder AlSi10Mg at section x = l/2 and at time moment (t = l$_{AB}$/2v) on top surface

Figure 35 shows the evolution of temperature at the position *P* as the heat source moves from position *A* to *B*. Error with respect to the FEM is under 2% throughout.
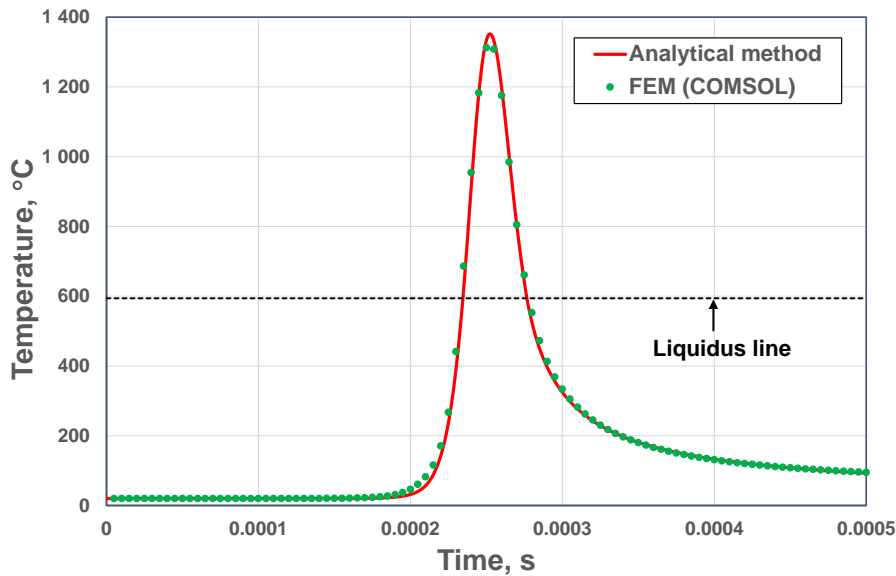

Figure 35 Temperature - time plot comparison between analytical method and FEM for selective laser melting of powder AlSi10Mg at position P (x = l/2 and y = w/2) on top surface

3.5   Case studies

Three cases were selected to demonstrate the applications of the proposed thermal model with history dependent thermal properties as described in the above section:

1) Case 1: LB-PBF process of AlSi10Mg
2) Case 2: LB-PBF process of IN 718
3) Case 3: EB-PBF process of IN 718

These cases can represent a wide range of both material properties and process conditions, which gives different thermal diffusivity in AlSi10Mg (higher) and in IN718 (lower). For the

case studies in this section, all thermal properties (thermal conductivity, specific heat and density) are considered to be temperature-dependent. Also, powder properties will be utilized in the case studies.

From a computational point of view, LB-PBF and EB-PBF are similar heating-cooling processes but with different heat sources and resulting build temperatures. The build components are subjected to a rapid heating and cooling cycle, with a high thermal gradient along their build direction. Another difference is that EB-PBF must have a preheating process. The main purpose of preheating is to prevent build failure caused by charging of powder particles by electrons, which is known as smoke. The preheating process is not modeled in the present model and only the initial temperature is set as input value. In the case of high preheating temperature, special treatment on thermal conductivity of powder is not necessary.

3.5.1 Case 1: LB-PBF process of AlSi10Mg

A nominal composition (Al-10%Si-0.3%Mg-0.3%Fe-0.08%Cu) was used to calculate specific heat and density by the CALPHAD method. The thermal conductivity of AlSi10Mg powder is taken from literature [18] as shown in Figure 29. The calculated temperature-dependent specific heat of AlSi10Mg powder using CALPHAD method are shown in Fig. 30a. For density of powder is evaluated using equation (28) assuming porosity as 0.5 below liquidus temperature (Fig. 30b). Table 7 lists the materials properties and process parameters for LB-PBF of powder AlSi10Mg.

Table 7 Materials properties and process parameters for selective laser melting of powder AlSi10Mg

Thermal conductivity (W/m·K)	See Figure 29 (powder)
Specific heat (J/kg·K)	See Figure 29a
Density (kg/m^3)	See Figure 29b (powder)
Liquidus temperature (°C)	594
Initial temperature (°C)	20
Laser velocity v (m/s)	2.0
Laser power (W)	100
spot size (μm)	80
Absorption	0.6

Figure 36 shows the top view of temperature contours at the time moment ($t = l_{AB}/2v$, position P) that the laser beam moves to a half-track length for selective laser melting of powder AlSi10Mg predicted by using analytical method (top) and FEM (bottom). It can be seen from Figure 36 that the melt pool has a more elongated tail ("comet tail profile" [5]) surrounded by recently solidified material compared to the case shown in Figures 31 and 33. This variation in temperature between the central molten material and the recently solidified material on the sides creates a temperature gradient. It is found that a good approximate contour was obtained after having special treatment on thermal conductivity.

Figure 37 shows temperature profile comparison between analytical method and FEM for selective laser melting of powder AlSi10Mg along the x-axis without and with special treatment on the thermal conductivity. A larger deviation in the tail of the heated zone is noted if no special treatment on the thermal conductivity as shown in Figure 37(a), resulting in a longer melt pool.
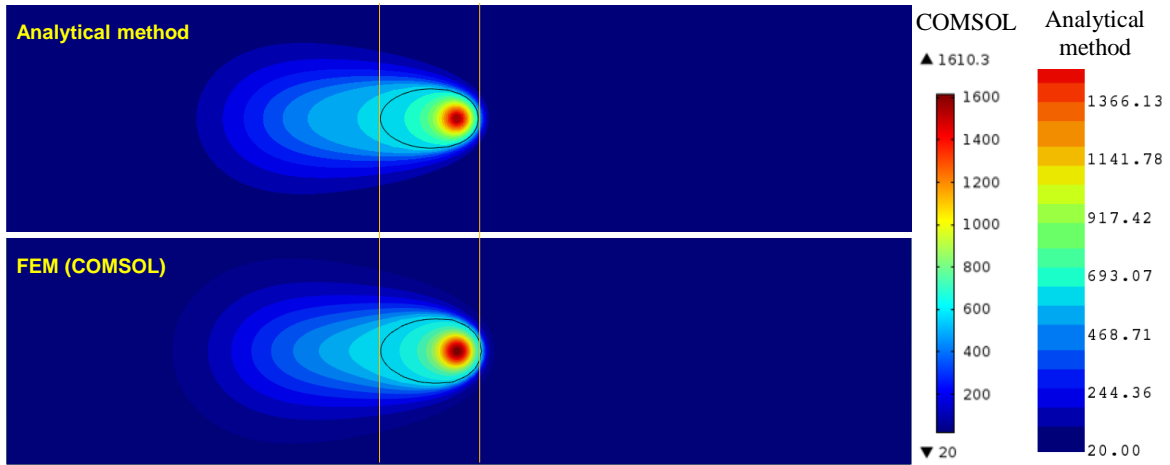
Figure 36 Top view of temperature profile (unit: °C) at the time moment (t = l$_{AB}$/2v) that the laser beam moves to a half-track length for selective laser melting of powder AlSi10Mg predicted by using analytical method (top) and FEM (bottom). The melt pool boundary is indicated by the solid black line.
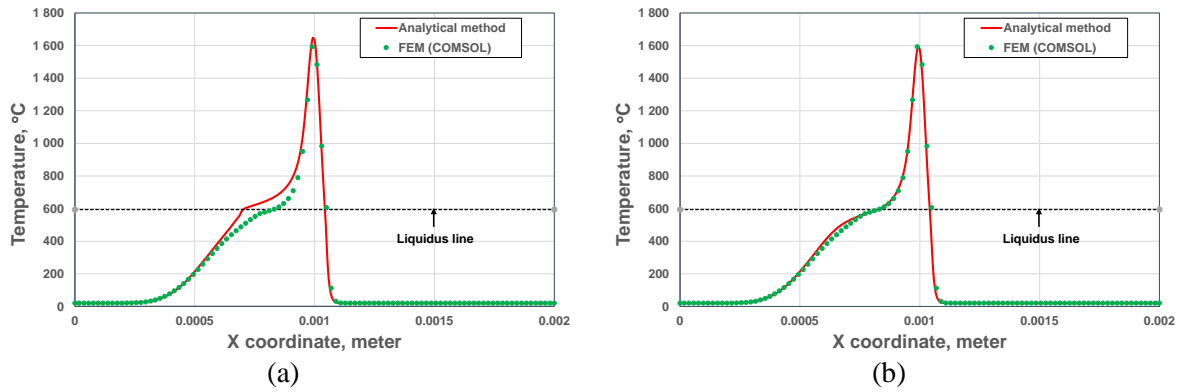

Figure 37 Temperature profile comparison between analytical method and FEM for LB-PBF of powder AlSi10Mg for section at y = w/2 and at time moment (t = l$_{AB}$/2v) on top surface: analytical method without (left) and with (right) modification for thermal conductivity.
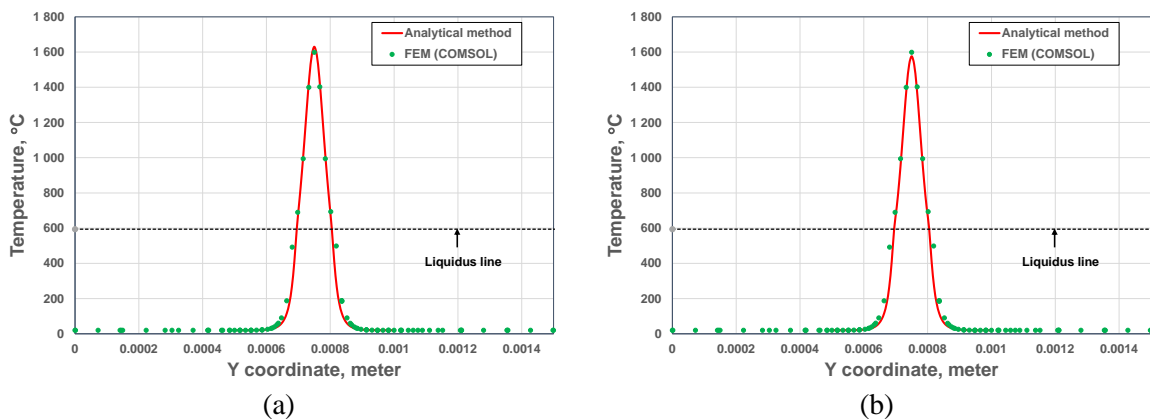

Figure 38 Temperature profile comparison between analytical method and FEM for LB-PBF of powder AlSi10Mg for section at x = l/2 and at time moment (t = l$_{AB}$/2v) on top surface: analytical method without (left) and with (right) modification for thermal conductivity.

Figure 38 shows temperature profile comparison between analytical method and FEM for LB-PBF of powder AlSi10Mg along the y-axis without and with special treatment on the thermal conductivity. As seen, the peak temperature drops slightly after special treatment on thermal

conductivity, which may be due to higher thermal conductivity. Otherwise, the special treatment on the thermal conductivity does not have much effect on the temperature profile distribution along the y-axis.
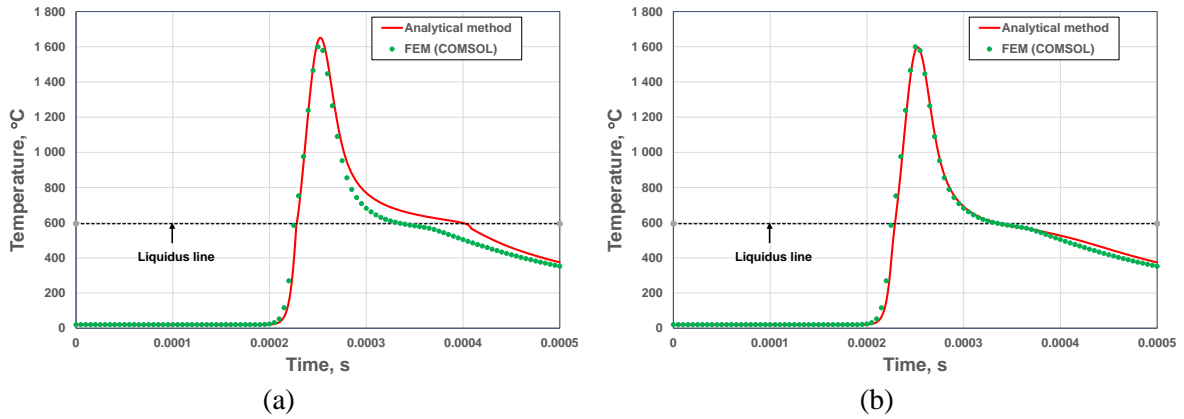

(a)   (b)

Figure 39 Temperature - time plot comparison between analytical method and FEM for LB-PBF of powder AlSi10Mg at position P (x = l/2 and y = w/2) on top surface: analytical method without (left) and with (right) modification for thermal conductivity.

A comparison of temperature histories between analytical model and FEM for selective laser melting of powder AlSi10Mg at position *P* (x = l/2 and y = w/2) on top surface is shown in Figure 39. There is a relatively larger deviation in temperature near liquidus line with the two methods without setting special treatment on thermal conductivity. However, a very good agreement for the predicted temperatures between analytical model and FEM is found when using special treatment on the thermal conductivity, which is of great significance for predicting solidification and the resulted microstructures. This gradient of curve after reaching the peak point also reflects the cooling rate. The cooling rate is of particular interest for predicting solidification and the resulting microstructure as well as any residual stress.

Figure 40 illustrates the temperature contour for LB-PBF of powder AlSi10Mg using cutting plane. The shape of 3D melt pool is clearly visualized as well.
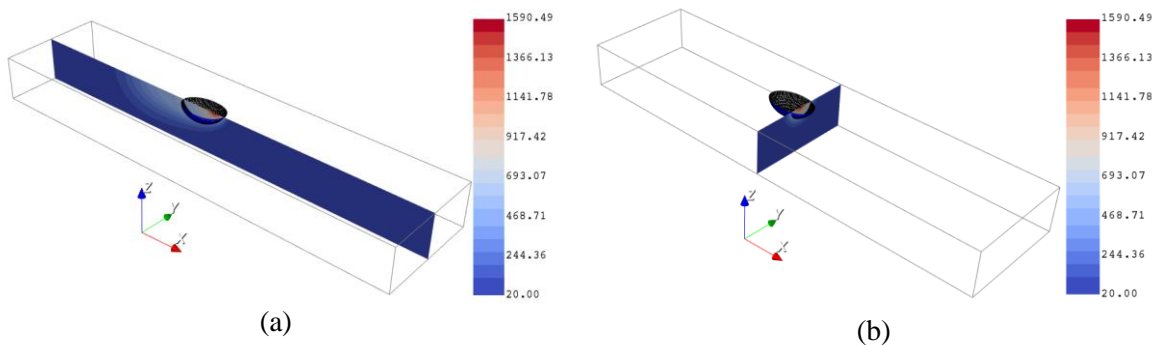

(a)   (b)

Figure 40 Temperature contour (unit: °C) for selective laser melting of powder AlSi10Mg using cutting plane: y-z plane (a) and x-z plane (b)

3.5.2 Case 2: LB-PBF process of INCONEL 718

In this case, the LB-PBF process of IN 718 powder was investigated. The thermal properties of powder A were calculated using CALPHAD method. The thermal conductivity of IN 718 powder is taken from literature [18] as shown in Figure 41. The calculated temperature-dependent specific heat of AlSi10Mg powder is shown in Figure 42a. For density of powder is obtained using equation (28) assuming porosity as 0.5 below liquidus temperature (Figure 42b).

Table 7 lists the materials properties and process parameters for selective laser melting of powder IN 718.
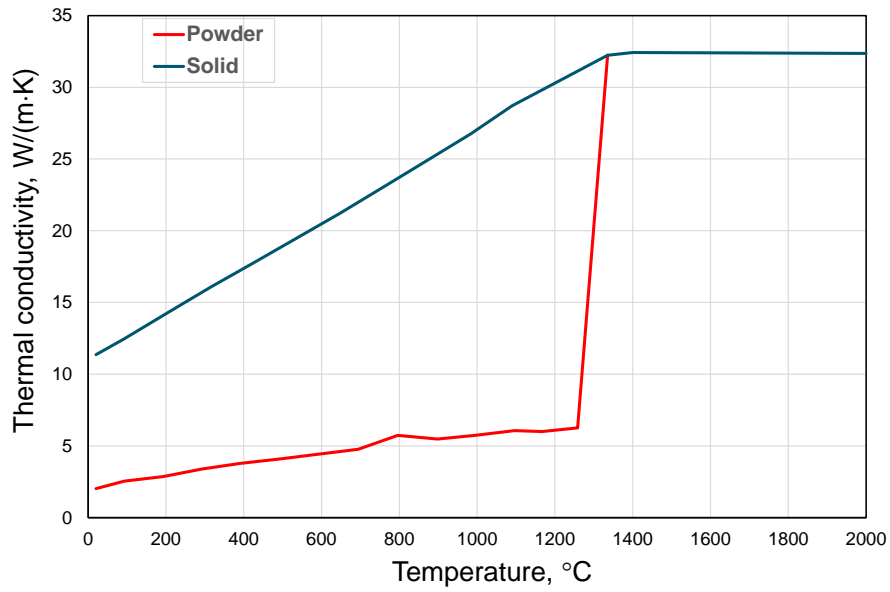

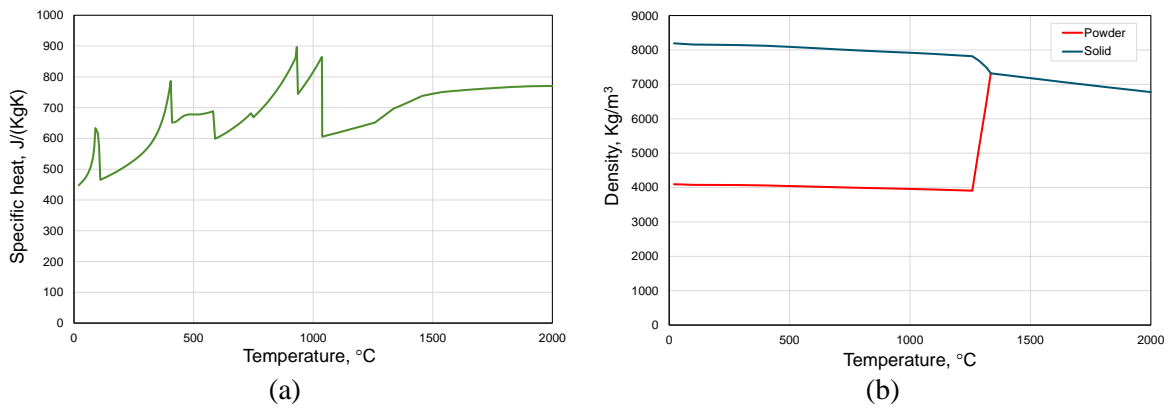*Figure 41 Temperature-dependent thermal conductivity of IN718 [17]*

Figure 42 Calculated temperature-dependent thermal properties of IN 718 powder using CALPHAD method: specific heat capacity (a) and density (b)

Table 8 Materials properties and process parameters for LB-PBF of powder IN 718

Thermal conductivity (W/m·K)	See Figure 29 (powder)
Specific heat (J/kg·K)	See Figure 29a
Density (kg/m^3)	See Figure 29b (powder)
Liquidus temperature (°C)	1335
Initial temperature (°C)	20
Laser velocity v (m/s)	1.0
Laser power (W)	100
spot size (µm)	100
Absorption	0.6

Figure 43 shows the top view of temperature contours at the time moment ($t = l_{AB}/2v$, position P) that the laser beam moves to a half-track length for LB-PBF of powder IN 718 predicted by using analytical method with treatment on thermal conductivity (top) and FEM (bottom). A relatively longer melt pool is seen as IN 718 powder has lower thermal diffusivity.
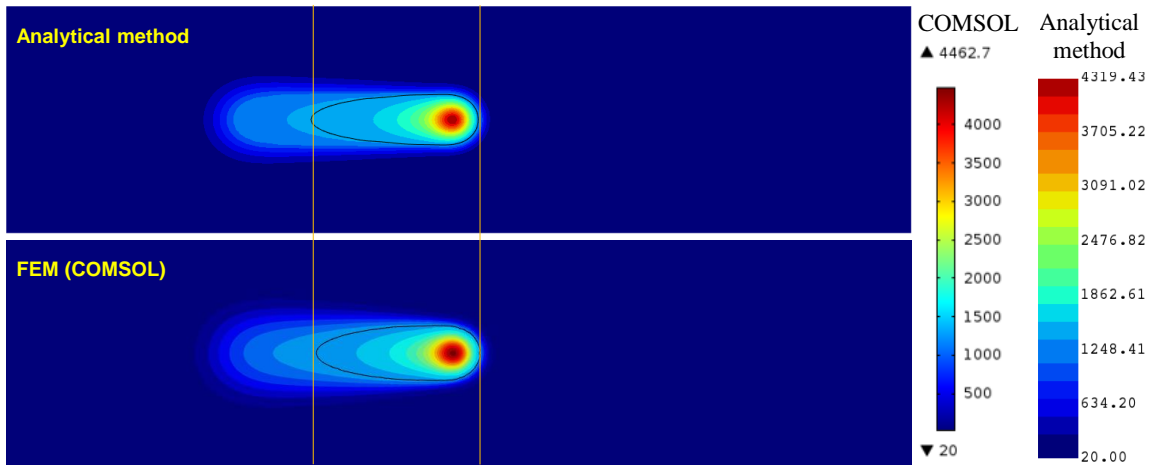

Figure 43 Top view of temperature profile (unit: °C) at the time moment ($t = l_{AB}/2v$) that the laser beam moves to a half-track length for LB-PBF of powder IN 718 predicted by using analytical method (top) and FEM (bottom). The melt pool boundary is indicated by the solid black line.
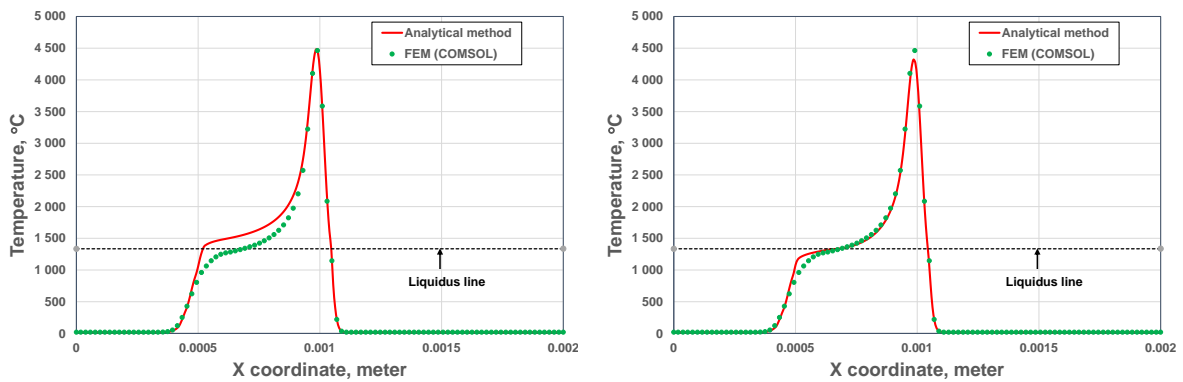

Figure 44 Temperature profile comparison between analytical method and FEM for LB-PBF of powder IN 718 for section at y = w/2 and at time moment ($t = l_{AB}/2v$) on top surface: analytical method without (left) and with (right) modification for thermal conductivity
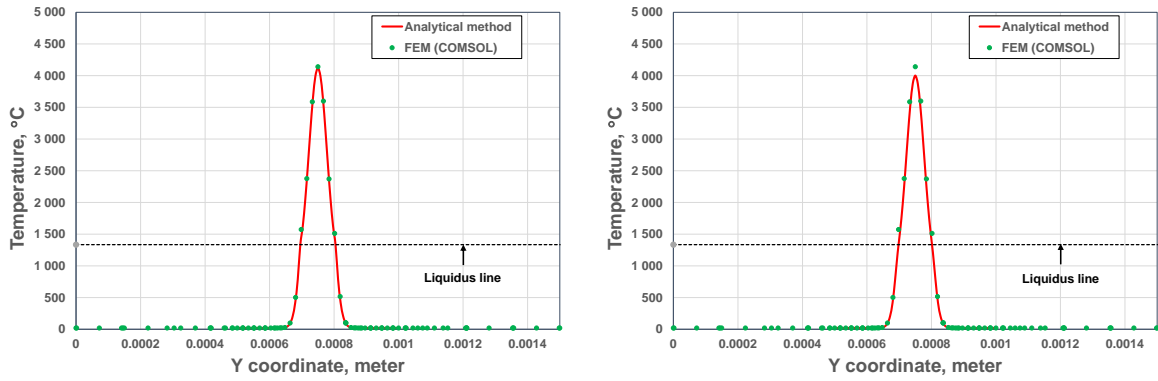
37

Figure 45 Temperature profile comparison between analytical method and FEM for LB-PBF of powder IN 718 for section at x = l/2 and at time moment (t = l$_{AB}$/2v) on top surface: analytical method without (left) and with (right) modification for thermal conductivity.

Figure 44 shows temperature profile comparison between analytical method and FEM for selective laser melting of powder IN 718 along the x-axis, without and with special treatment on the thermal conductivity, respectively. The special treatment on the thermal conductivity can only modify the temperature deviation above the liquidus line in the so-called comet tail zone as shown in Figure 44b. This can be explained with the fact that the beam starts from the position A (x = 0.0005 m). Similar results for temperature profile along the y-axis as Case 1 are shown in Figure 45.

A comparison of temperature histories between analytical method and FEM for selective laser melting of powder IN 718 at position P (x = l/2 and y = w/2) on top surface is shown in Figure 46. The analytical method can predict temperature as good as FEM in this case (Figure 46b).

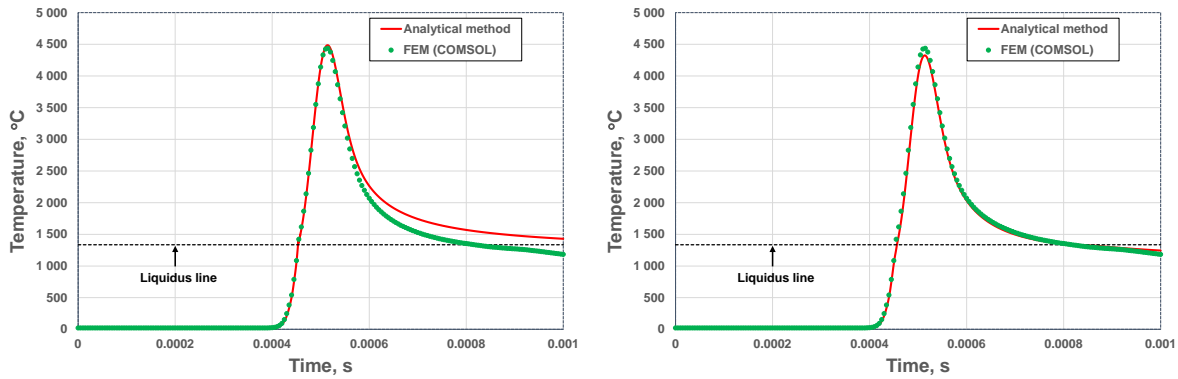The 3D melt pool is shown together with cutting place in Figure 47.

Figure 46 Temperature - time plot comparison between analytical method and FEM for LB-PBF of powder IN 718 at position P (x = l/2 and y = w/2) on top surface: analytical method without (left) and with (right) modification for thermal conductivity.
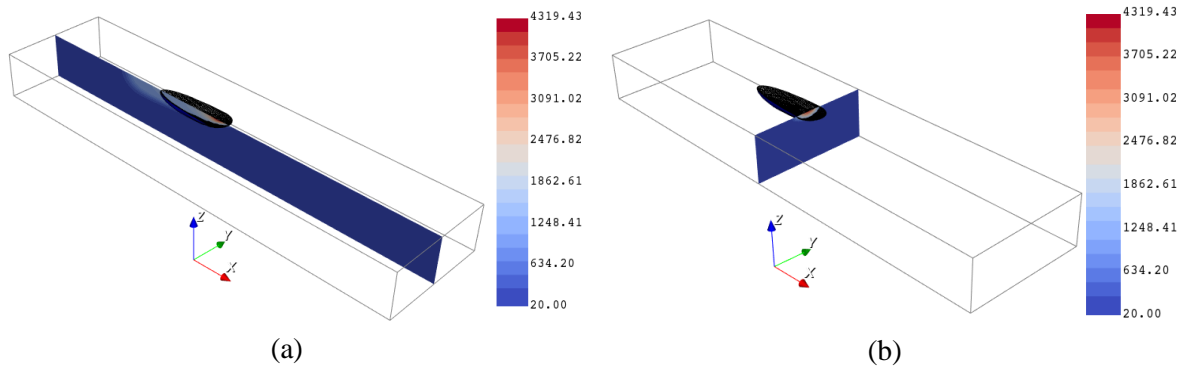
Figure 47 Temperature contour (unit: °C) using cutting plane: y-z plane (a) and x-z plane (b) for LB-PBF of powder IN 718.

3.5.3　Case 3: EB-PBF process of INCONEL 718

In Case3, the EB-PBF process of IN 718 powder was investigated. The entire domain is subjected to a predefined field corresponding to the preheating temperature. The materials properties and process parameters for EB-PBF of powder IN 718 are given in Table 9. The preheating temperature is critical to the solid-state sintering, which is mainly determined by the material property and affected by the size of powder.

Figure 48 gives a comparison of melt pool geometries and spatial temperature distributions between analytical method and FEM. It is seen that result by the analytical method is obviously close to the one by the finite element method. This consistence is also presented for other results, like temperature profiles along *x* axis (Figure 49) and *y* axis (Figure 50) as well temperature history (Figure 51). As mentioned before, no special treatment on thermal conductivity of powder is done for the case of high preheating temperature.

Table 9 Materials properties and process parameters for EB-PBF of powder IN 718

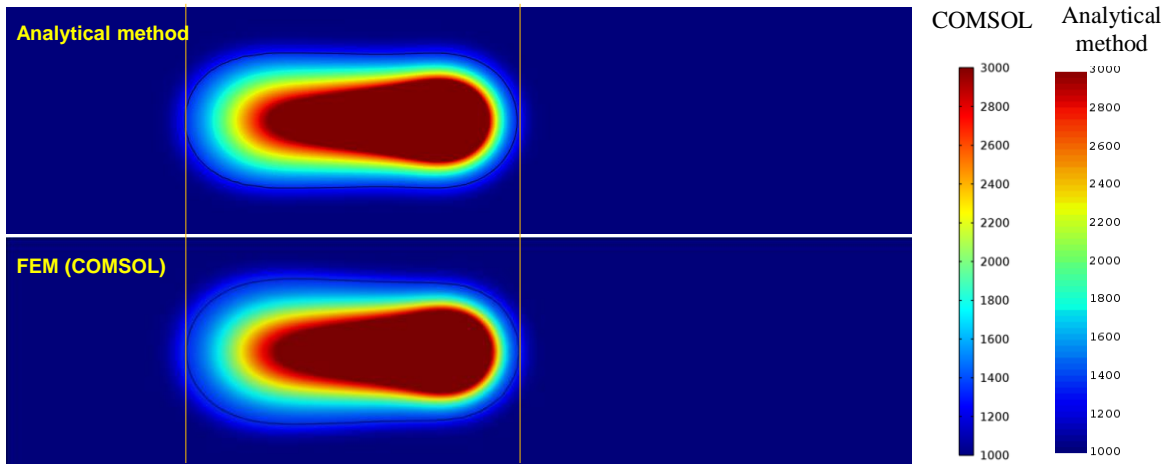| Thermal conductivity (W/m·K)	See Figure 29 (powder)
Specific heat (J/kg·K)	See Figure 29
Density (kg/m^3)	See Figure 29 (powder)
Liquidus temperature (°C)	1335
Initial temperature (°C)	1000
Beam velocity *v* (m/s)	2.0
Beam power (W)	600
spot size (μm)	200
Absorption	0.8

Figure 48 Top view of temperature profile (unit: °C) at the time moment (t = l_{AB}/2v) that the electron beam moves to a half-track length for EB-PBF of powder IN 718 predicted by using analytical method (top) and FEM (bottom). The melt pool boundary is indicated by the solid black line.
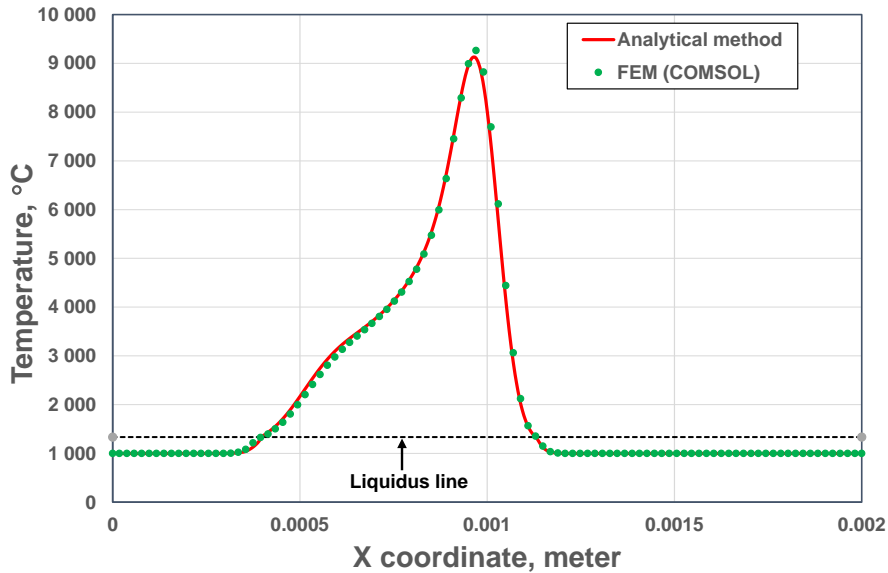

Figure 49 Temperature profile comparison between analytical method and FEM for EB-PBF of powder IN 718 for section at y = w/2 and at time moment (t = l_{AB}/2v) on top surface.

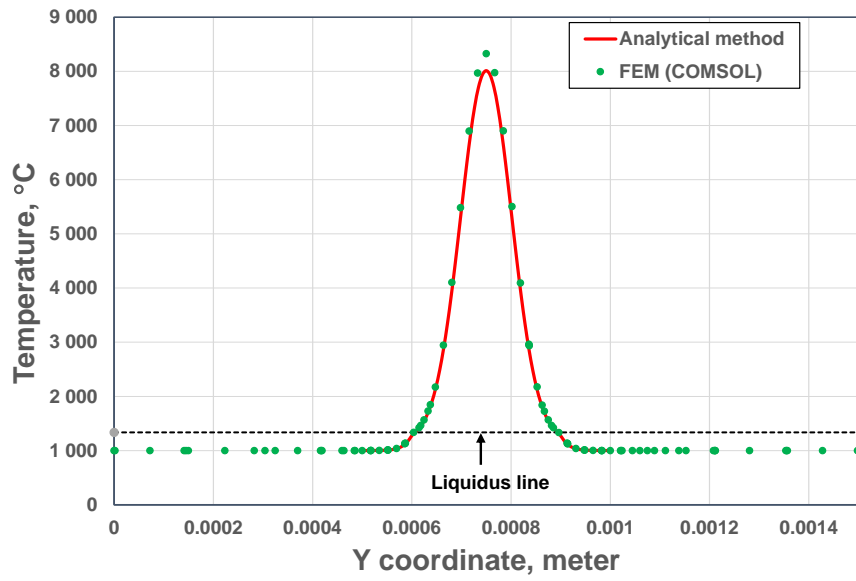*Figure 50 Temperature profile comparison between analytical method and FEM for EB-PBF of powder IN 718 at section x = l/2 and at time moment (t = l$_{AB}$/2v) on top surface.*

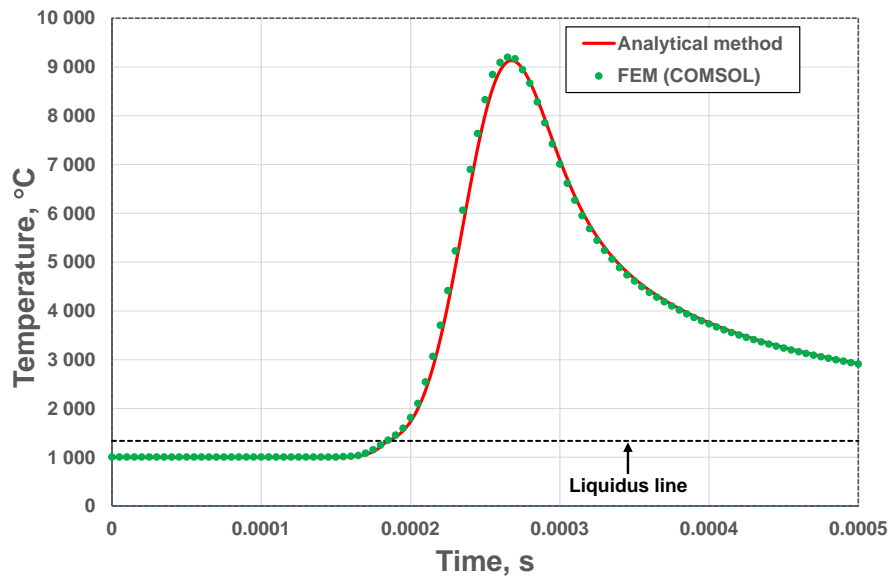*Figure 51 Temperature - time plot comparison between analytical method and FEM for EB-PBF of powder IN 718 at position P (x = l/2 and y = w/2) on top surface*

4   A robust and fast modeling tool for AM

At Swerim AB, solidification modeling has been the research hotspot. A robust and fast modeling tool for AM (MicAM) has been developed based on our many year's experiences for the property modeling and graphical user interface (GUI). MicAM stands for Microstructure modeling in Additive Manufacturing process. In the present work, the analytical model was implemented as an additional module "Process Modeling (PBF)" in the MicAM software.

4.1   Graphical User Interface of MicAM

Logo:

Two modules are currently available in MicAM software: Property Modeling, Process Modeling (PBF). Figure 52 shows the opening interface of MicAM, in which Property module is seen first.

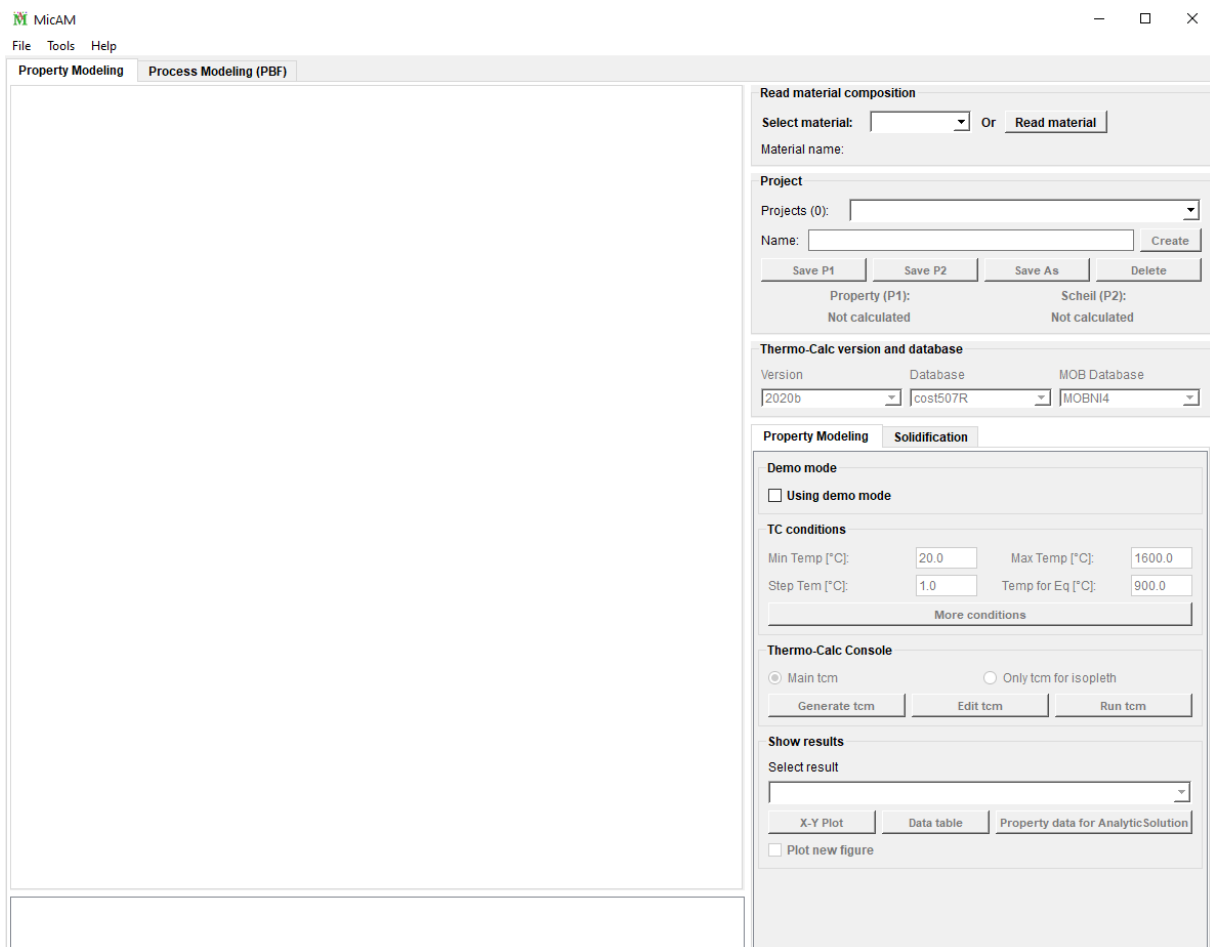*Figure 52 Opening interface of MicAM and property module*

4.2   Main features

4.2.1   Property modeling module

This module (see Figure 52) is constructed to prepare and execute calculation of properties for solid material based on CALPHAD engine (like commercial software Thermo-Calc).

For the property module, the following features are available:

1) Selection of Thermo-Calc version and databases

2) Generation and modification of Thermo-Calc macro file
3) Execution of thermodynamic calculation (run Thermo-Calc Console)
4) Plotting and export of selected results
    a. Variation of phase fractions with temperature
    b. Solidification path
    c. Liquidus and solidus temperature
    d. Density, enthalpy, heat capacity, thermal conductivity (depending on database), etc.

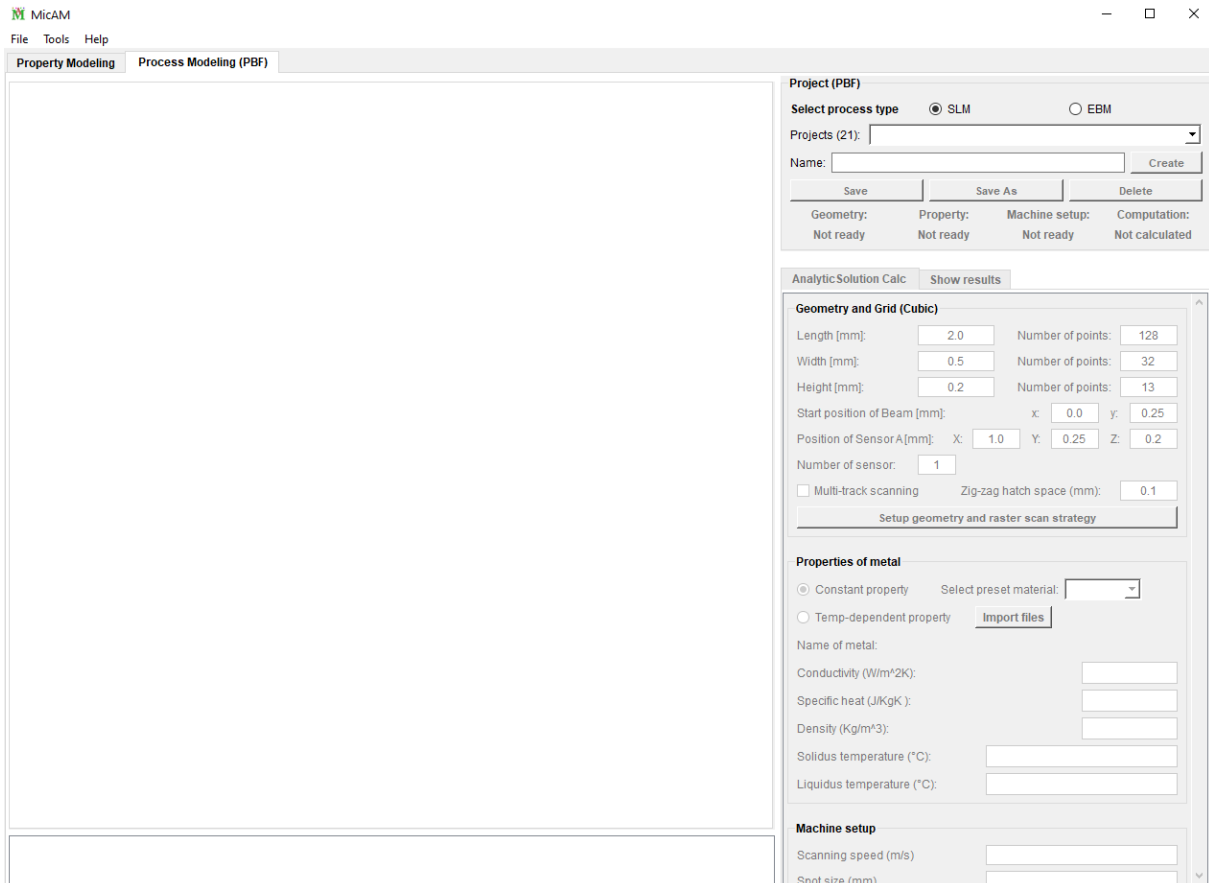The calculated thermal properties can be used directly for process modeling of PBF.

Figure 53 Process modelling module of MicAM

4.2.2 Process modeling (PBF) module

For the process modeling module (see Figure 53), following features are available:

1) Setup of raster and temperature sensor.

    It allows to set the dimension of powder domain, starting position of beam and zigzag track, and positions of temperature sensors.

2) Set temperature-dependent thermal properties (using prepared files) or constant property values.

    It reads prepared thermal properties from pre-defined text file for thermal conductivity, specific heat, and density for both powder and solid states.

3) Set process parameters.

    The process parameters include scanning speed, beam spot size, beam power, absorptivity, and initial temperature.

43

4) Plotting and exporting of selected results:
   a) Contour of 3D temperature field at different times;
   b) Temperature - time curves at specified sensor positions;
   c) 3D visualization of melt pool, digitally measured dimension values (length, width and height;
   d) Temperature profile along a specified path (x-axis, y-axis).

A cutting plane contour is plotted as in Figure 54 if selecting "Show cutting plane". Furthermore, a 3D melt pool is drawn if selecting "show liquidus isotherm". More functions can be used, for example to pan rotate and zoom the object using shift key plus left mouse, only left mouse, and wheel, respectively.
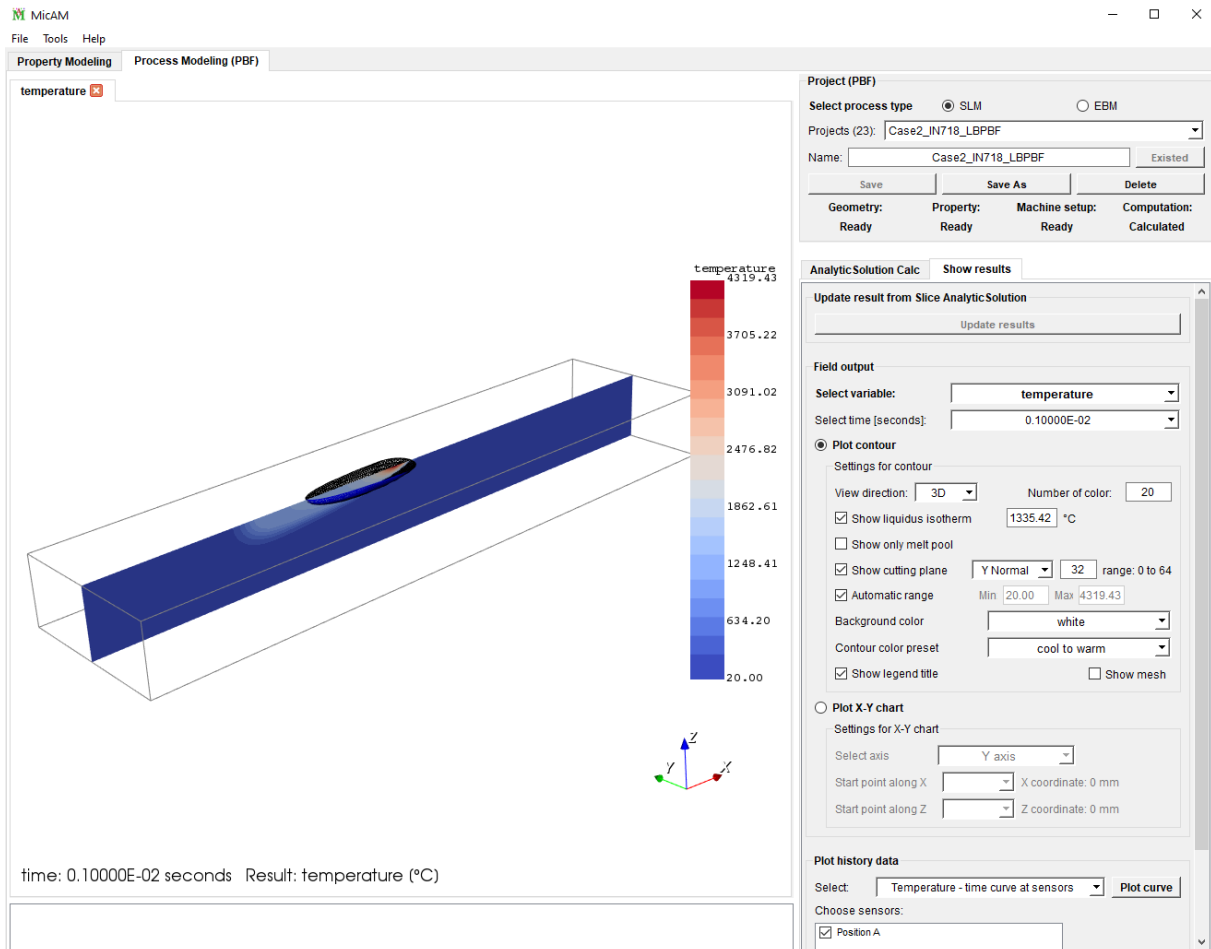
Figure 54 A cutting plane contour and 3D melt pool at specified time.

4.3   Use of MicAM

MicAM uses currently Thermo-Calc Console to calculate thermal properties and related values. It requires licenses for Thermo-Calc and related databases. The open-source code Open Calphad will be possibly added as calculation engine in the future.

A Step-by-step guide is prepared to help the users get started quickly. The demo version of MicAM is freely available for the Swedish industries. Currently, the material property data for two materials (AlSi10Mg and IN718) are prepared in the MicAM software.

5   Concluding remarks

The major achievements in the current project are concluded as follows:

1) Standard procedure is established for measuring the thermal properties of powder material using LFA 457 apparatus. Netzsch Proteus software is further used for evaluating measurements, resulting pulse and temperature signals vs time curves.

2) Transient finite element models have been formulated to identifying material properties and process parameters by using commercial software COMSOL Multiphysics®. The identification method involves the inverse heat conduction problem solution of a real experiment. It should also be noted that combining the heat transfer model with the built-in parametrical identification in one simulation process provides a simple and fast solution to account for a large variety of heat transfer phenomena.

3) A time-efficient thermal model of PBF AM was built by semi-analytical approach. The model was applied to predict the localized-transient thermal history, temperature field as well as 3D melt pool geometry. The semi-analytical model was validated by a commercial finite element software (COMSOL). An adapted algorithm for applying temperature-dependent thermal properties for powder materials in the thermal model was utilized, resulting in a more reasonable prediction.

4) The developed approach also demonstrated the ability to predict the thermal behavior of powder in AM process associated with the current state of material, which is determined by the property - temperature relation. From this perspective, the proposed method can be easily applied to the process development stage to reject faulty process conditions considering temperature - dependent material properties. From an industrial point of view, this approach can save time and resources with respect to the selection and evaluation of AM powder. The resulted temperature histories and gradients can be easily used for modeling solidification, phase transformation and microstructure evolution.

5) The developed thermal model was implemented in the computational tool (MicAM software) for AM process. The integrated software facilitates the property calculation, modeling work and the further parameter studies. The results can be visualized in three dimensions, and the size of the molten pool at any scanning time can be measured. In this sense MicAM can help manufacturers quickly and accurately make important evaluations in their products design and development phases.

Future work:

  1) To predict the thermal behavior of powder in AM process associated with the current state of material, which is determined by the maximum temperature value in the past temperature history.
  2) To develop advanced parallel algorithm to speed-up the computation.
  3) To apply for more alloy powders.

Knowledge dissemination:

A 3-hour knowledge dissemination online workshop on the robust method for powder thermal property testing and thermal modeling in additive manufacturing will be organized by Swerim AB. The workshop includes property measurement method, MicAM software as well as its use. The intention is for the participants from Swedish AM companies to get started with MicAM and be potential co-developers.

6   Acknowledgement

7   References

[1]. [Online]. Available: https://cio-wiki.org/wiki/Additive_Manufacturing_(AM)

[2]. J. Romano, L. Ladani and M. Sadowski, Thermal Modeling of Laser Based Additive Manufacturing Processes within Common Materials, Procedia Manufacturing, 1 (2015), pp. 238 - 250.

[3]. M. Markl, C. Körner, Multiscale modeling of powder bed-based additive manufacturing, Annu. Rev. Mater. Res. 46 (1) (2016) 93 - 123. http://dx.doi.org/10.1146/annurev-matsci-070115-032158 .

[4]. B. Schoinochoritis, D. Chantzis and K. Salonitis, Simulation of metallic powder bed additive manufacturing processes with the finite element method: A critical review, Proceedings of the Institution of Mechanical Engineers Part B, Journal of Engineering Manufacture, 231 (2017), pp. 96 - 117.

[5]. Z. Luo, Y. Zhao, A survey of finite element analysis of temperature and thermal stress fields in powder bed fusion Additive Manufacturing, Additive Manufacturing, 21 (2018), pp. 318 - 332.

[6]. P. Stavropoulos and P. Foteinopoulos, Modelling of additive manufacturing process: a review and classification, Manufacturing Rev., 2 (2018), pp. 1 – 26.

[7]. A. Razavykia, E. Brusa, C. Delprete, R. Yavari, An Overview of Additive Manufacturing Technologies - A Review to Technical Synthesis in Numerical Study of Selective Laser Melting, - Materials, 2020 - mdpi.com.

[8]. P. Ninpetch, P. Kowitwarangkul, S. Mahathanabodee, P. Chalermkarnnon, and P. Ratanadecho, A review of computer simulations of metal 3D printing, AIP Conference Proceedings 2279, 050002 (2020); https://doi.org/10.1063/5.0022974 .

[9]. H.L. Wei, T. Mukherjee, W. Zhang, J.S. Zuback, G.L. Knapp, A. De, T. DebRoy, Mechanistic models for additive manufacturing of metallic components, Progress in Materials Science, 116 (2021), 100703.

[10]. I.A. Roberts, C.J. Wang, R. Esterlein, M. Stanford, and D.J. Mynors, A three-dimensional finite element analysis of the temperature field during laser melting of metal powders in additive layer manufacturing, International Journal of Machine Tools and Manufacture, 49 (2009), pp. 916 - 923.

[11]. Y. Li and D. Gu, Parametric analysis of thermal behavior during selective laser melting additive manufacturing of aluminum alloy powder, Materials & Design, 63 (2014), pp. 856 - 867.

[12]. F. Thümmler, Fritz, and O. Rainer, An introduction to powder metallurgy, Vol. 490. London: Institute of Materials, 1993.

[13]. Y. Du, X. You, F. Qiao, L. Guo, and Z. Liu. A model for predicting the temperature field during selective laser melting, Results in Physics, 12 (2019), pp. 52 - 60.

[14]. R. Andreotta, L. Ladani, and W. Brindley, Finite element simulation of laser additive melting and solidification of Inconel 718 with experimentally tested thermal properties, Finite Elements in Analysis and Design, 135 (2017), pp. 36 - 43.

[15]. E. R. Denlinger, G. Michael, I. Jeff, and M. Pan, Thermomechanical model development and in situ experimental validation of the Laser Powder-Bed Fusion process, Additive Manufacturing, 16 (2017), pp. 73 - 80.

[16]. S.S. Sih, J.W. Barlow, The prediction of the emissivity and thermal conductivity of powder beds, Particul. Sci. Technol, 22 (4) (2004), pp. 427 - 440.

[17]. P. Promoppatum, S.C. Yao, P. C. Pistorius, and A. D. Rollett, A comprehensive comparison of the analytical and numerical prediction of the thermal history and solidification microstructure of Inconel 718 products made by laser powder-bed fusion, Engineering, 3 (2017), pp. 685 - 694.

[18]. Z. Li, B. Li, P. Bai, B. Liu, and Y. Wang, Research on the thermal behaviour of a selectively laser melted aluminium alloy: simulation and experiment, Materials, 11 (2018), pp. 1172.

[19]. A. Plotkowski, M.M. Kirka, S.S. Babu, Verification and validation of a rapid heat transfer calculation methodology for transient melt pool solidification conditions in powder bed metal additive manufacturing, Additive Manufacturing, 18 (2017), pp. 256 - 268, doi: 10.1016/j.addma.2017.10.017.

[20]. B. Stump, A. Plotkowski, an adaptive integration scheme for heat conduction in additive manufacturing, Applied Mathematical Modelling, 75 (2019), pp. 787 - 805.

[21]. E. Mirkoohi, *et al*., Thermal Modeling of Temperature Distribution in Metal Additive Manufacturing Considering Effects of Build Layers, Latent Heat, and Temperature-Sensitivity of Material Propertie, J. Manuf. Mater. Process, 2 (2018), pp. 63; doi:10.3390/jmmp2030063.

[22]. J. Ning, S. Y. Liang, Analytical Modeling of Three-Dimensional Temperature Distribution of Selective Laser Melting of Ti-6Al-4V. Preprints 2018, 2018090101 (doi: 10.20944 /preprints 201809.0101.v1).

[23]. R. Forslund, A. Snis, S. Larsson, Analytical solution for heat conduction due to a moving Gaussian heat flux with piecewise constant parameters, Applied Mathematical Modelling, 66 (2019), pp. 227 - 240.

[24]. J. C. Steuben, A. J. Birnbaum, J. G. Michopoulos, A. P. Iliopoulos, Enriched analytical solutions for additive manufacturing modeling and simulation, Additive Manufacturing, 25 (2019), pp. 437 - 447.

[25]. Y. Huang, Comprehensive Analytical Modeling of Laser Powder-Bed/Fed Additive Manufacturing Processes and an Associated Magnetic Focusing Module, PhD Thesis, University of Waterloo, 2019.

[26]. B. Liu, F. Gang, and L. Lei, An analytical model for rapid predicting molten pool geometry of selective laser melting (SLM), Applied Mathematical Modelling, 92 (2021), pp. 505 - 524.

[27]. Juan J. Valencia and Peter N. Quested, ASM Handbook, Volume 15: Casting, ASM Handbook Committee, pp. 468 - 481, 2008.

[28]. K. C. Mills, Recommended values of thermophysical properties for selected commercial alloys, Woodhead Publishing, 2002.

[29] T. DebRoy, H.L. Wei, J.S. Zuback, T. Mukherjee, J.W. Elmer, J.O. Milewski, *et al*. Additive manufacturing of metallic components - process, structure and properties, Prog Mater Sci, 92 (2018), pp. 112 - 224

[30]. T. Nolan, Y. Lian, and M. Sussman, Development of simulation tools for selective laser melting additive manufacturing, In Solid Freeform Fabrication 2017, Proceedings of the 28th Annual International Solid Freeform Fabrication Symposium, 2017.

[31]. F. Thümmler, R. Oberacker, An Introduction to Powder Metallurgy. Cambridge, London: The University Press, 1993.

[32]. H. Czichos T. Saito, L.E. Smith, editors. Springer Handbook of Materials Measurement Method, 1st ed. New York, Springer Science & Business Media, 2006, pp. 1208. DOI: 10.1007/978‐3‐540‐30300‐8.

[33]. L. Wei, L. E. Ehrlich, M. J. Powell-Palm, C. Montgomery, J. Beuth, and J. A. Malen, Thermal conductivity of metal powders for powder bed additive manufacturing, Additive Manufacturing, 21 (2018), pp. 201 - 208.

[34]. B. Cheng B, B. Lane, J. Whiting, K. Chou, A Combined Experimental-Numerical Method to Evaluate Powder Thermal Properties in Laser Powder Bed Fusion, ASME. J. Manuf. Sci. Eng., 140 (2018), 111008-1 to 111008-8.

[35]. S. Zhang, B. Lane, J. Whiting, K. Chou, On thermal properties of metallic powder in laser powder bed fusion additive manufacturing, Journal of manufacturing processes, 47 (2019), pp. 382 - 392.

[36]. Martínez-Maradiaga, D., Mishin, O.V. & Engelbrecht, K. Thermal Properties of Selectively Laser-Melted AlSi10Mg Products with Different Densities. J. of Materi Eng and Perform, 29 (2020), pp .7125 - 7130.

[37]. C.J. Smith, Tammas-Williams, E. Hernandez-Nava, and I. Todd, Tailoring the thermal conductivity of the powder bed in Electron Beam Melting (EBM), Additive Manufacturing, Scientific reports, 7 (2017), pp. 1 - 8.

[38]. A. Hope and P. Mason, Applying computational thermodynamics to additive manufacturing, MRS Bulletin, 44 (2019), pp. 156 - 157.

[39]. https://thermocalc.com/content/uploads/Documentation/Databases/Thermodynamic/tcal-examples-collection.pdf

[40]. https://www.sentesoftware.co.uk/

[41]. Markus Uhlirsch, Comparison of IN718 powders from different producers in the electron beam powder bed fusion additive manufacturing process (EB-PBF), Master's thesis, University of Bremen and Swerim AB, 2019.

[42]. W. J. Parker, R. J. Jenkins, C. P. Butler, G. L. Abbott, J. Appl. Phys., 32 (1961), pp. 1679 - 1684.

[43]. https://www.netzsch-thermal-analysis.com/en/products-solutions/thermal-diffusivity-conductivity/lfa-457-microflash/

[44]. https://comsol.com/

[45]. https://cantera.org/

[46] T.W. Eagar, N.-S. Tsai, Temperature fields produced by traveling distributed heat sources, Weld. J., 62 (12) (1983), pp. 346 - 355.

[47] N.T. Nguyen, A. Ohta, K. Matsuoka, N. Suzuki, Y. Maeda, Analytical solutions for transient temperature of semi-infinite body subjected to 3-D moving heat sources, Weld. Res., Suppl., 78.R (1999), pp. 265 - 274.